



DIPLOMARBEIT

Investigation of erosion properties of mixed tungsten and boron layers relevant for nuclear fusion devices

ausgeführt am Institut für Angewandte Physik der Technischen Universität Wien Wiedner Hauptstraße 8-10 / E134 1040 Wien, Österreich

unter der Anleitung von

Dipl.-Ing.in Martina Fellinger, BSc

und

Univ.Prof. Dr.techn. Friedrich Aumayr

durch

Raphael Gurschl, BSc Matrikelnummer 11901867

Wien, am 14.05.2025		
	Raphael Gurschl	Friedrich Aumayr



Abstract

Plasma-facing materials in fusion reactors are exposed to extremely harsh conditions. They have to withstand high temperatures and bombardment of energetic particles, escaping from the confined plasma. Tungsten was selected as first wall material for ITER (International Thermonuclear Experimental Reactor) due to its favorable properties, such as high melting point and comparatively low sputter yield. One goal of ITER, like any fusion reactor, is to maximize energy output. To improve plasma performance and reduce impurities like oxygen, wall conditioning techniques such as boronization are employed. This process involves the injection of a gas containing boron into the vessel, followed by a glow discharge that decomposes the gas, resulting in the deposition of a thin layer of boron on the reactor wall. This layer modifies the erosion properties of the wall.

This thesis investigates how the erosion behavior changes with varying boron concentration. To accomplish this, five different samples consisting of intermixed tungsten and boron at various concentration ratios were examined. This thesis focused on the angle dependent sputter yield of the desired materials under 2 keV Ar⁺ and 2 keV D₂⁺ irradiation. The experimental studies were conducted using a quartz crystal microbalance (QCM), a device capable of detecting mass changes down to $10 \,\mathrm{pg}\,\mathrm{cm}^{-2}\,\mathrm{s}^{-1}$. Additional binary collision approximation (BCA) simulations, utilizing the code SDTrimSP, were carried out to provide comparison between simulation and experiments. In addition to measuring the sputter yield, atomic force microscopy (AFM) was employed to provide information about possible changes to the surface when subjected to ion beam irradiation. The characterization of the surface before and after the irradiation was achieved by extracting parameters such as the root-mean-square roughness value (RMS) and the mean of the surface inclination angle distribution (SIAD) from the AFM images.

This study showed that under the bombardment of 2 keV Ar^+ and 2 keV D_2^+ the eroded mass decreased with increasing boron concentration of the target. Simultaneously, the number of sputtered tungsten particles decreased while the number of sputtered boron particles increased, a beneficial outcome for fusion reactors, as high-Z impurities pose a significant risk to plasma performance.

Kurzfassung

Plasmanahe Materialien in Fusionsreaktoren sind extremen Bedingungen ausgesetzt. Sie müssen hohen Temperaturen und dem Beschuss energiereicher Teilchen, die aus dem eingeschlossenen Plasma entweichen, standhalten. Aufgrund seines hohen Schmelzpunkts und der vergleichsweise niedrigen Sputterrate wurde Wolfram als Wandmaterial im ITER (International Thermonuclear Experimental Reactor) ausgewählt. Ein Ziel von ITER, wie eines jeden Fusionsreaktors, ist es, die Energieausbeute zu maximieren. Um die Plasmaleistung zu verbessern und Verunreinigungen wie Sauerstoff zu reduzieren, werden Wandkonditionierungstechniken wie die Boronisierung angewendet. Bei diesem Verfahren wird ein borhaltiges Gas in den Reaktorbehälter eingeleitet, gefolgt von einer Glimmentladung, die das Gas zersetzt, was zur Ablagerung einer dünnen Borschicht auf der Reaktorwand führt. Diese Schicht verändert die Erosionseigenschaften der Wand.

Diese Arbeit untersucht den Einfluss unterschiedlicher Borkonzentrationen auf das Erosionsverhalten von Wolfram-Bor-Mischungen anhand von fünf Proben mit variierenden Mischungsverhältnissen. Insbesondere konzentrierte sich die Arbeit auf die winkelabhängige Sputterrate der gewünschten Materialien unter 2 keV Ar⁺ und 2 keV D₂⁺ Bestrahlung. Die experimentellen Untersuchungen wurden mit einer Quarzkristall-Mikrowaage (QCM) durchgeführt, einem Gerät, das Massenänderungen bis zu 10 pg cm⁻² s⁻¹ erfassen kann. Zusätzlich wurden Simulationen mit dem Code SDTrimSP durchgeführt, um einen Vergleich zwischen Simulation und Experiment zu ermöglichen. Neben der Messung der Sputterrate wurde Rasterkraftmikroskopie (AFM) eingesetzt, um mögliche Veränderungen der Oberfläche unter Ionenbeschuss zu analysieren. Die Charakterisierung der Oberfläche vor und nach der Bestrahlung erfolgte durch die Auswertung von Parametern wie dem quadratischen Mittelwert der Rauheit (RMS) und dem Mittelwert der Verteilung des Oberflächenneigungswinkels (SIAD) aus den AFM-Bildern.

Diese Arbeit zeigte, dass unter dem Beschuss mit $2 \,\mathrm{keV} \,\mathrm{Ar}^+$ und $2 \,\mathrm{keV} \,\mathrm{D}_2^+$ die erodierte Masse mit steigender Borkonzentration des Targets abnahm. Gleichzeitig nahm die Anzahl der gesputterten Wolfram Partikel ab, während die Anzahl des gesputterten Bor Partikel zunahm, was für einen Kernfusionsreaktor vorteilhaft ist, da Verunreinigungen mit hoher Massenzahl Z ein erhebliches Risiko für die Plasmaleistung darstellen.



Contents

1	Intr	roduction 1
	1.1	Fusion
		1.1.1 Thermonuclear fusion process
		1.1.2 Tokamak principle
		1.1.3 First wall and boronization 6
		1.1.4 Motivation
2	The	eory 9
	2.1	Quartz crystal microbalance (QCM)
	2.2	Sputter yield calculations
	2.3	Simulations
3	Exp	perimental setup and data processing 13
	3.1	QSPARX
	3.2	Measurement procedure
	3.3	Data post-processing
	3.4	QMS
	3.5	ĀFM
4	San	aple characterization 23
	4.1	Sample compositions
	4.2	Surface properties
		r · r
5		ults and discussion 27
	5.1	Pure tungsten
		5.1.1 Sputter yield
		5.1.2 Surface changes
	5.2	Pure boron
		5.2.1 Sputter yield
		5.2.2 Surface changes
	5.3	$W:B \approx 1:1 \dots \dots 37$
		5.3.1 Sputter yield
		5.3.2 Surface changes
		5.3.3 QMS measurements

5.4	$W:B \approx 4:1 \dots \dots$						
	5.4.1	Sputter yield	41				
	5.4.2	Surface changes	42				
	5.4.3	QMS measurements	43				
5.5	W:B ≈	st 1:4	45				
	5.5.1	Sputter yield	45				
	5.5.2	Surface changes	46				
	5.5.3	QMS measurements	47				
5.6	Compa	arison and summary	48				
	5.6.1	Sputter yield	48				
	5.6.2	Surface changes	54				
	5.6.3	QMS measurements	55				
Con	clusio	and outlook	57				
Bibliography							
	5.5 5.6	5.4.1 5.4.2 5.4.3 5.5 W:B ≈ 5.5.1 5.5.2 5.5.3 5.6 Compa 5.6.1 5.6.2 5.6.3 Conclusion	$5.4.1 \text{Sputter yield} \\ 5.4.2 \text{Surface changes} \\ 5.4.3 \text{QMS measurements} \\ 5.5 \text{W:B} \approx 1:4 \\ 5.5.1 \text{Sputter yield} \\ 5.5.2 \text{Surface changes} \\ 5.5.3 \text{QMS measurements} \\ 5.6 \text{Comparison and summary} \\ 5.6.1 \text{Sputter yield} \\ 5.6.2 \text{Surface changes} \\ 5.6.3 \text{QMS measurements} \\ \\ \text{Conclusion and outlook} \\ \\ \text{Conclusion and outlook} \\$				

Introduction

The world as we know it today is confronted with unique challenges. The uninterrupted increase in global temperature can be attributed to the production of greenhouse gases, such as water vapour or carbon dioxide (CO₂) [1]. These gases accumulate in the atmosphere and reflect infrared radiation coming from Earth, thus contributing to global warming [2]. Nevertheless, the emission of CO₂ continues to increase (see Figure 1). The rate of increase in emissions has slowed in the last years, but has not reached its peak yet.

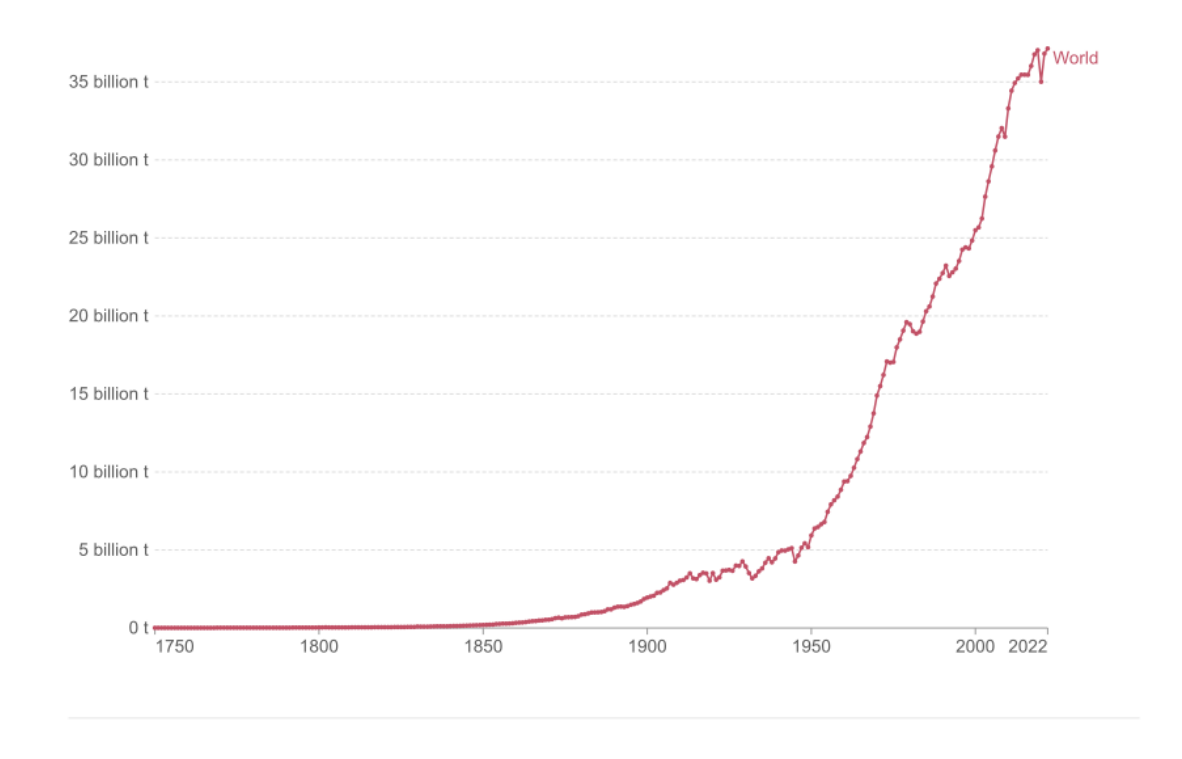


Figure 1: The annual carbon dioxide emissions from the combustion of fossil fuels and industry. Taken and adapted from [3].

A significant contributor to CO₂ emissions is the generation of electricity from fossil fuels, such as coal, gas and oil (see Figure 2).

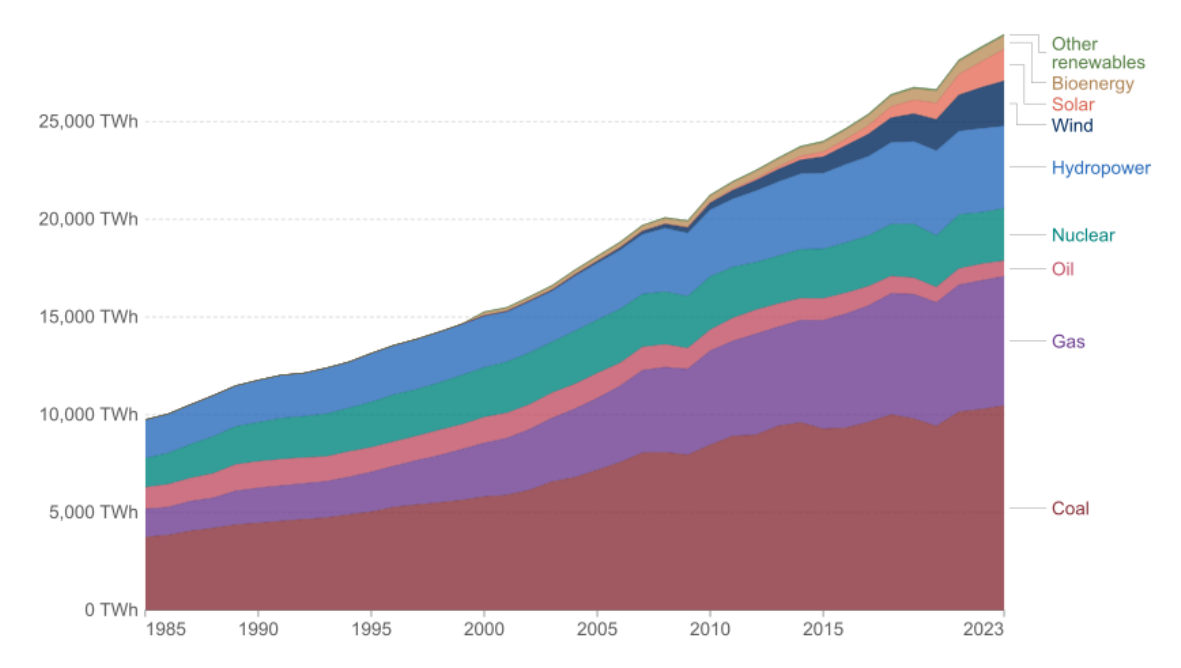


Figure 2: An overview of the global energy production by individual sources. Taken and adapted from [4].

In order to simultaneously reduce the emission of greenhouse gases from fossil fuel-powered power plants and still provide sufficient energy, new methods of energy production must be developed. One potential solution is the development of renewable energy sources, such as wind, solar, and hydro power. However, these power plants are dependent on natural factors that are beyond human control, and therefore cannot be relied upon to contribute to a constant energy production. One potential source of this constant energy production could be a nuclear fusion facility, which relies on the fusion of deuterium and tritium. More information about the fusion reaction is given in subsection 1.1.1. Such a power plant would have a number of advantages over conventional energy sources. First, the fusion reaction would result in no CO_2 emissions. Second, the fuels required for nuclear fusion are largely available on Earth, as deuterium can be extracted from seawater, while tritium can principally be produced during operation via breeding blankets. Third, a fusion power plant is not dependent on geographical location or weather conditions. Fourth, in contrast to a conventional fission power plant, a fusion power plant would have almost no long-term radioactive waste. These are just a few of the advantages that a fusion power plant would possess. In the next chapter, a brief introduction about fusion processes is given.

1.1 Fusion

1.1.1 Thermonuclear fusion process

In contrast to fission, which involves the splitting of a nucleus to form two smaller nuclei, fusion is the process of combining two nuclei to form a heavier nucleus, accompanied by the release of energy in the form of kinetic energy of the products. The energy released is a consequence of the fact that the mass of the resulting nucleus is less than the sum of the masses of the initial nuclei. The missing mass is converted to kinetic energy according to $E = \Delta mc^2$. The smaller mass of the fused nucleus can be explained by the higher binding energy of the product, as illustrated in Figure 3.

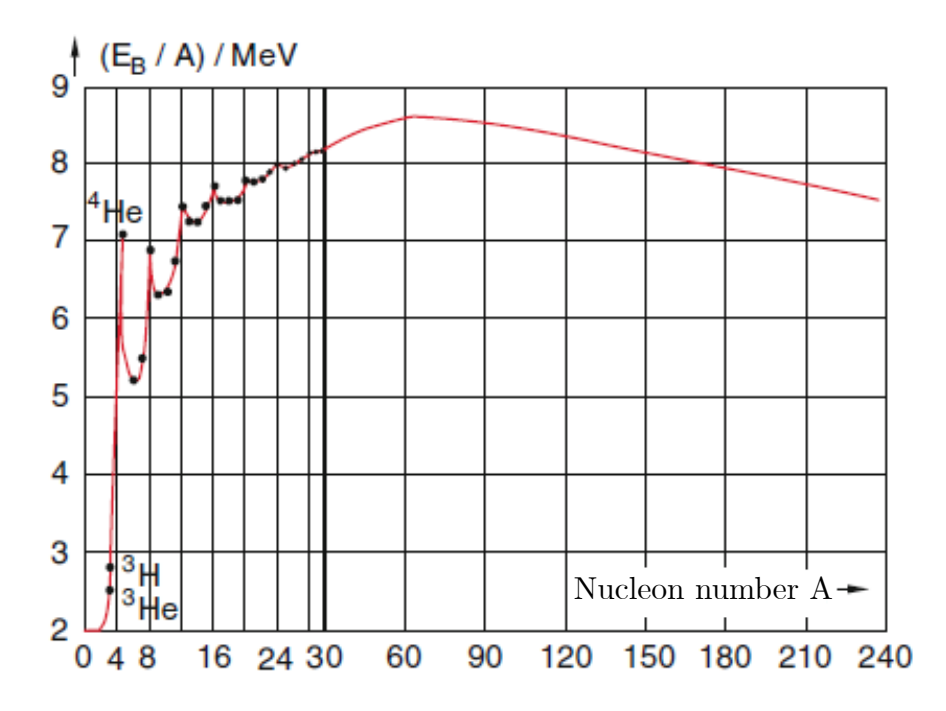


Figure 3: Average binding energy per nucleon as a function of nucleon number. Taken and adapted from [5].

Figure 3 shows that the isotope nickel-62 (⁶²Ni) has the highest binding energy per nucleon. The binding energy can be increased coming from the left side of the graph through fusion, and from the right side through fission. Fusion processes are observed in stars like our sun, where the proton-proton chain reaction is the most dominant fusion process. Within this reaction chain, a deuterium nucleus, a positron and an electron are generated, while kinetic energy is released.

$$p + p \rightarrow {}_{1}^{2}D + e^{+} + \nu_{e} + 0.42 \,\text{MeV}$$
 (1.1)

However, due to the relatively low cross-section (probability) of this reaction, it is not feasible to efficiently perform this process on Earth. In thermonuclear fusion, the most effective process is deuterium-tritium fusion, due to its high reaction rate, comparably low ignition temperature and high energy release. The equation

$${}_{1}^{2}D + {}_{1}^{3}T \rightarrow {}_{2}^{4}He + {}_{0}^{1}n + 17.59 \,\text{MeV}$$
 (1.2)

represents the reaction between a deuterium and a tritium nucleus, which results in the formation of a helium nucleus and a neutron, accompanied by the release of 17.59 MeV in the form of kinetic energy of the products. Each reaction product incorporates kinetic energy according to its relative mass. The idea is that the kinetic energy from the neutron can ultimately be used to generate electricity. A visual representation of the deuterium-tritium fusion process can be seen in Figure 4. The relevant force that initiates the fusion process shown in Figure 4 is

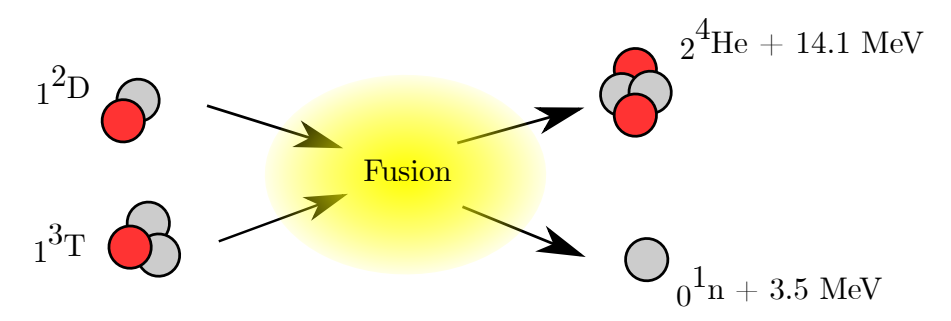


Figure 4: Visual representation of the deuterium-tritium fusion.

the strong interaction. As this force is very short-ranged and positively charged nuclei repel each other due to the long-ranged electromagnetic force, the particles must first overcome this Coulomb barrier in order for the fusion process to start. In order to effectively overcome this barrier, the atoms must posses a high energy level and a high collision rate to create enough reaction probability. The high energy is provided by a temperature of $\approx 100 \cdot 10^6$. Consequently, any discussion of the thermonuclear fusion process must include plasma physics. Plasma, which is often referred to as the fourth state of matter, exhibits a form where the electrons and nuclei move independently. From the Saha Equation

$$\frac{n_{\rm i}}{n_{\rm n}} \approx 2.4 \cdot 10^{21} \frac{T^{3/2}}{n_{\rm i}} e^{-U_{\rm i}/k_{\rm b}T}$$
(1.3)

the ratio of the densities of ionized atoms n_i to neutral atoms n_n in a gas is rising with the temperature T in Kelvin [6]. Here k_b represents Boltzmann's constant and U_i the ionization energy for this gas. Therefore, with rising temperature the ionization level increases, and the gas is fully ionized at the working temperature



of a fusion power plant. Additionally, for a self sustaining fusion device the Lawson criterion, or triple product,

$$n \cdot \tau_{\rm E} \cdot T \ge 5 \cdot 10^{21} \,\mathrm{m}^{-3} \mathrm{keVs},\tag{1.4}$$

must be satisfied [7]. n represents the density, T the temperature and $\tau_{\rm E}$ the energy confinement time of the plasma. The energy confinement time is defined as the time it takes for a system to decrease from an initial energy W_0 to $\frac{1}{e} \cdot W_0$.

As a fusion process occurs only with a certain probability, not every interaction between nuclei results in a fusion process. Therefore, the hot plasma has to be confined. If not confined, the created plasma would cool down and scatter immediately. There are a number of potential methods for achieving confinement, with magnetic confinement being the most advanced approach.

1.1.2 Tokamak principle

One possible configuration for the achievement of magnetic confinement is the tokamak. The term itself is a Russian acronym and can be translated to toroidal chamber with magnetic coils. The total magnetic field necessary for the confinement consists of different individual magnetic fields. A toroidal magnetic field is generated by toroidal field coils surrounding the vessel (see Figure 5).

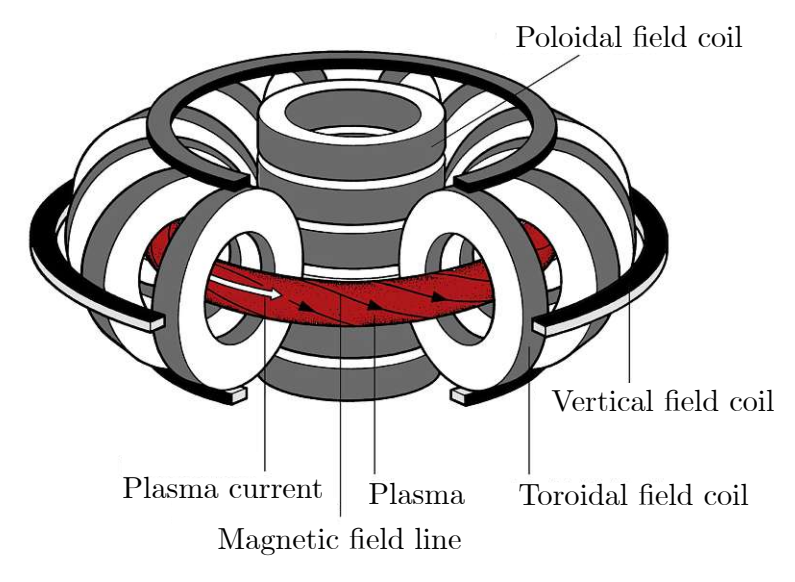


Figure 5: Principle of magnetic confinement in a tokamak. Taken and adapted from [8].



The inner poloidal field coils serve as the primary winding of a transformer, while the plasma itself constitutes the secondary winding. A current is induced in the plasma, thereby creating a poloidal magnetic field. The combination of these two fields results in twisted and helical magnetic field lines, permitting the compensation of the vertical drift. To ensure a stable plasma configuration, it is necessary to introduce an additional vertical magnetic field component. This forms the baseline of any magnetic field configuration in a tokamak [7].

1.1.3 First wall and boronization

The first wall in a fusion reactor is an expression for the surface in the vessel that is in direct contact with the plasma. Materials must posses specific properties in order to be applicable as first wall materials. They must be able to withstand high heat fluxes, ion bombardment and the resulting erosion and chemical composition changes. Tungsten has proven to be a potential first wall material and will be used as a first wall and divertor material in the fusion reactor ITER, which is currently under construction. The divertor is a material structure in a fusion device, where magnetic field lines end and therefore has to cope with an extreme flux of particles and heat. A cross-sectional view of the ITER tokamak is provided in Figure 6, with particular emphasis on the divertor and the first wall facing the plasma.

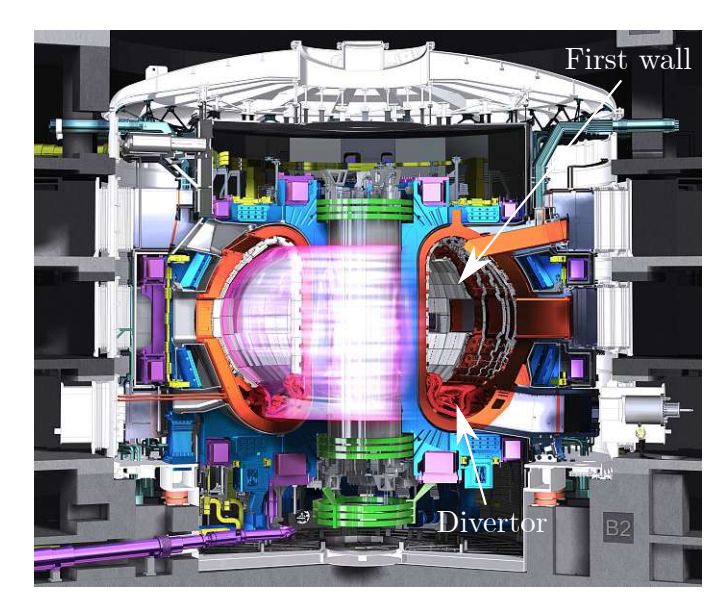


Figure 6: Cross-sectional view of ITER with the divertor and the first wall highlighted. Taken and adapted from [9].



Tungsten as a first wall material has several advantageous properties when compared to other materials. These include a high melting point, low sputter yield, and high thermal conductivity. It was also found in some cases that tungsten reduces the oxygen content in the vessel in comparison to one equipped with graphite tiles [10]. Nevertheless, in order to achieve more favorable plasma conditions the amount of oxygen must be further reduced.

One method for reducing the oxygen content in a fusion device is through the utilization of a process known as boronization. This describes the deposition of a thin layer of boron on the first wall of the reactor. One potential approach to achieve this deposition is by performing a glow discharge with the gas diborane B₂D₆ [11]. The boron layer acts as an oxygen getter by binding residual oxygen to boron, forming boron oxide (BO) [12]. As demonstrated in numerous examples, this technique leads to significantly improved confinement times and a reduction in oxygen and carbon impurities present in the plasma [13–16]. As boronization is planned for the operation of future fusion reactors, it is necessary to understand the impact of boron layers in respect to the erosion properties of the first wall.

1.1.4 Motivation

As discussed in the previous section, boronization will be employed during operation in an all-metal device, e.g. in the case of ITER with a full tungsten wall. During the process of boronization, a thin layer of boron is added to the first wall. This alters the composition of the surface that is in contact with the plasma. This thesis is concerned with identifying potential differences in sputter yield that may result from this surface change in the first wall. Sputter yield measurements of pure tungsten were performed in the past and function as a reference in this thesis [17-19].

To simulate the change in the first wall composition, several samples with different mixing ratios of tungsten and boron are under investigation. The angle dependent sputter yield of the samples is measured via a quartz crystal microbalance (QCM). The used QCM, which is described in more detail in section 2.1 and chapter 3, allows measuring mass changes down to $10 \,\mathrm{pg}\,\mathrm{cm}^{-2}\,\mathrm{s}^{-1}$ [20]. Additionally to the commencement of the experiments, binary collision approximation (BCA) simulations are conducted in order to give a comparison with the experimental results (see chapter 5). The findings of this work will be of importance in the near future, given that ITER is a full tungsten device that will operate with boronization.

Theory

Quartz crystal microbalance (QCM)

One way of obtaining information about the sputter yield is to detect tiny changes in mass. One method of observing these mass changes is a technique involving a quartz crystal microbalance (QCM). This method relates mass changes Δm of a system to eigenfrequency changes Δf via the Sauerbrey equation [21]

$$\frac{\Delta f}{f_{\rm Q}} = -\frac{\Delta m}{m_{\rm Q}} = -\frac{\Delta m}{A_{\rm Q} \cdot d_{\rm Q} \cdot \rho_{\rm Q}},\tag{2.1}$$

where $f_{\rm Q}$ denotes the initial eigenfrequency, $m_{\rm Q}$ the initial mass, $A_{\rm Q}$ the area, $d_{\rm Q}$ the thickness and ρ_Q the density of the quartz. This equation remains valid if a sufficiently thin layer is deposited on the quartz, which makes it suitable to our application |21|.

The QCM used in this study was developed at the Institute of Applied Physics (IAP) of TU Wien |22|. Two gold electrodes with $\approx 100 \,\mathrm{nm}$ thickness were deposited on the quartz crystal. The desired target material is then deposited as a thin film on top of one gold electrode. One can then drive a shear mode thickness oscillation at the system's resonance frequency $f_{\rm Q}$. An illustration of the QCM setup can be seen in Figure 7.

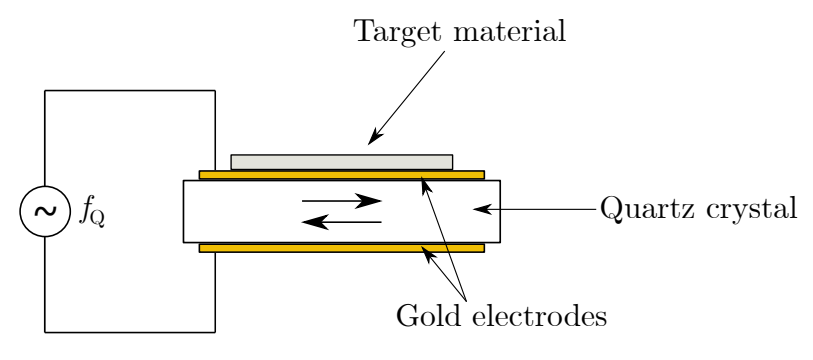


Figure 7: Illustration of the QCM setup.

The resonance frequency of the QCM is approximately 6 MHz. In practice, the oscillations are driven by an alternating voltage applied to the quartz, which induces a mechanical deformation due to the piezoelectric effect. During particle bombardment, changes in the resonance frequency Δf are tracked, while the initial eigenfrequency $f_{\rm Q}$ can be determined prior to conducting the measurement. Further details regarding the electronics that are used to track the resonance frequency are provided in chapter 3. The change in frequency can then be translated into mass according to equation (2.1). A detailed explanation of the sputter yield calculation is presented in the subsequent section.

Another important aspect regarding the QCM is the quartz sensitive area. Inside the sensitive area mass changes lead to significant changes of the eigenfrequency. It has been observed that the sensitivity decreases radially outwards from the center [21]. The sensitivity is directly related to the squared shear amplitude of the quartz, which corresponds to a Gaussian function [23]. The function that describes the sensitivity of a quartz is depicted in Figure 8. In conclusion, it is necessary to irradiate the quartz within the designated sensitive area to induce measurable mass changes.

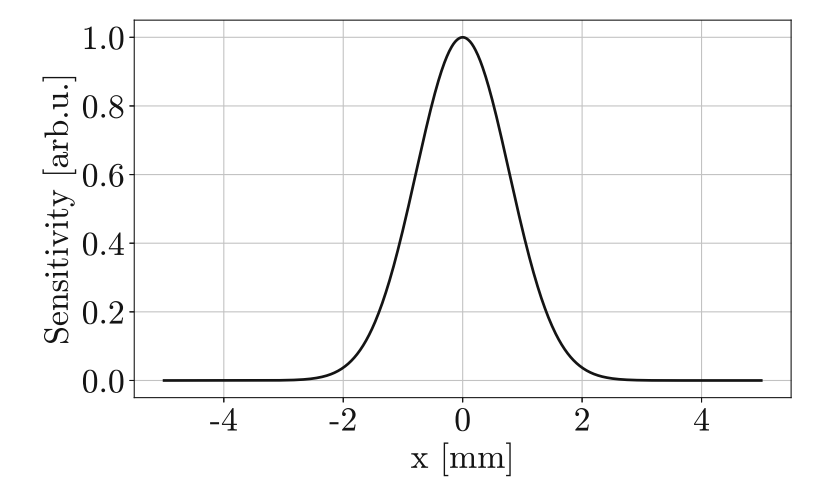


Figure 8: Sensitivity of a quartz used in this thesis as a function of distance from the center. Data taken from [24].

2.2 Sputter yield calculations

In this application it is advantageous to calculate the sputter yield as

$$Y = \frac{\text{mean number of sputtered atoms}}{\text{incident ion}}.$$
 (2.2)

In order to determine this quantity, it is first practical to introduce a sputter yield in terms of atomic mass change per impinging ion

$$y = -\frac{\Delta m_{\rm amu}}{N_{\rm ions}},\tag{2.3}$$

with $\Delta m_{\rm amu}$ being the atomic mass change per cm² and $N_{\rm ions}$ the number of ions per cm² hitting the target. Substituting equation (2.1) into the definition of the atomic mass change per cm² yields

$$\Delta m_{\text{amu}} = \frac{\Delta m}{A_{\text{Q}} \cdot m_0} = -\frac{\Delta f \cdot m_{\text{Q}}}{A_{\text{Q}} \cdot m_0 \cdot f_{\text{Q}}} = -\frac{\Delta f \cdot d_{\text{Q}} \cdot \rho_{\text{Q}}}{m_0 \cdot f_{\text{Q}}}, \tag{2.4}$$

with $m_0 = 1.66 \cdot 10^{-27}$ kg being the atomic mass unit.

The number of impinging ions per cm^2 , denoted by N_{ions} , can be calculated using the ion current density j(t) within a time interval $t \in [t_1, t_1 + \Delta t]$, the charge state q of the ion and the elementary charge e_0 .

$$N_{\text{ions}} = \frac{1}{q \cdot e_0} \int_{t_1}^{t_1 + \Delta t} j(t)dt \tag{2.5}$$

If the current density is assumed to be constant over time, that is, if j(t) = j =const, $\forall t \in [t_1, t_1 + \Delta t]$, equation (2.5) simplifies to

$$N_{\rm ions} = \frac{j \cdot \Delta t}{q \cdot e_0}.$$
 (2.6)

Putting equations (2.4) and (2.6) into equation (2.3) results in

$$y = \frac{\Delta f}{\Delta t} \cdot \frac{1}{j} \cdot \frac{d_{\mathcal{Q}} \cdot \rho_{\mathcal{Q}} \cdot q \cdot e_0}{m_0 \cdot f_{\mathcal{Q}}},\tag{2.7}$$

an expression for the sputter yield in terms of atomic mass units per incident ion. If a pure target composition is assumed, the sputter yield Y can be calculated by dividing y by the atomic target mass $m_{\rm T}$, giving

$$Y = \frac{y}{m_{\rm T}} = \frac{\Delta f}{\Delta t} \cdot \frac{1}{j} \cdot \frac{d_{\rm Q} \cdot \rho_{\rm Q} \cdot q \cdot e_0}{m_0 \cdot f_{\rm Q} \cdot m_{\rm T}} = \frac{\Delta f}{\Delta t} \cdot \frac{1}{j} \cdot C, \tag{2.8}$$

which is an expression for the mean number of sputtered target atoms per incident ion, where C is a material constant [17, 18, 20, 22].



2.3 Simulations

One aspect of this thesis concerns the comparison of simulated and experimental data (see chapter 5). In this section, a brief introduction of the simulation program used is provided.

The program utilized for the simulations is SDTrimSP Version 7.02, a tool developed at the Max Planck Institute for Plasma Physics (IPP) [25]. The software successfully unifies the dynamic collision program TRIDYN and the static collision program TRIM. The terms "static" and "dynamic" refer to the composition of the target, when it is subjected to particle bombardment. In the static case, the composition remains unaltered throughout the simulation in contrast to the dynamic case.

SDTrimSP simulates atomic collisions and is capable of calculating ranges, reflection coefficients and sputtering yields for different angles of incidence, different projectile and target species. It can also provide information on depth distributions of implanted atoms and energy distributions of back-scattered and sputtered atoms. The program employs the binary collision approximation (BCA). This implies that only atomic two-body collisions occur. The projectiles travel on straight paths between elastic collisions and lose energy due to electronic stopping in between. Further details regarding the BCA and the two initial programs can be found in [26].

The most recent version of the software introduces the option of selecting crystalline target structures. This is a significant improvement since the simulations for tungsten samples did not fully correspond to the experimental results in recent studies [18]. One potential explanation for this discrepancy is the presence of crystalline structures in the targets. This topic will be further discussed in chapter 5.

Experimental setup and data processing

In order to perform sputter yield measurements, it is first necessary to establish an appropriate experimental setup. A dedicated experimental setup already exists at the Institute of Applied Physics (IAP) at TU Wien. This chapter provides an overview of the Qcm based SPuttering And Retention experiment (QSPARX) that was utilized in this study. In addition, it offers insight into the measurement procedure and the subsequent data processing.

As the samples are subjected to atomic force microscopy (AFM) before and after irradiation, an explanation of the measurement principle is given at the end of this chapter. To avoid any potential misinterpretation, the term 'AFM' will be employed to denote both the microscope and the associated technique.

3.1 QSPARX

In order to perform sputter yield measurements, it is essential that the environmental conditions are well understood and precisely controllable. Therefore, the experiments were conducted in ultra-high vacuum conditions of approximately 10^{-9} mbar. This minimizes contaminations and enables the creation and acceleration of ions. At the QSPARX, the vacuum is achieved by a pre-vacuum scroll pump and two turbomolecular pumps. The reduction of adsorbates such as water inside the experimental chamber can be achieved by baking of the entire chamber walls after the chamber has been exposed to air in the course of venting.

Once the required environmental conditions are met, one can bombard a desired target material on the QCM with atoms to induce mass changes. Due to the difficulty in controlling neutral atoms, ions are utilized for targeting a specific location, as their path can be easily modified by electric and magnetic fields and their impact energy can be precisely controlled. At the QSPARX, the ions are generated by a SPECS IQE 12/38 ion source. The desired atom species is supplied in gaseous form to the ion source. In this study, the selected ions were deuterium D_2^+ and argon Ar⁺. Deuterium was chosen because it is one of the two fuel species in nuclear

fusion reactors. Argon is used as a seeding gas in fusion reactors to protect the wall from high heat loads [27]. It is expected that both ion species are contributing to sputtering of wall materials. The desired gas is introduced into a mixing volume, and subsequently into the ion source by means of a thermovalve, which enables controlling of the gas pressure. Following the supply of the selected gas, ionization occurs through collisions with electrons emitted by a thorium coated tungsten filament. The ions are then extracted and accelerated to achieve the desired kinetic energy.

Subsequently, the ions undergo selection and shaping. Firstly, a Wien filter is employed, utilizing a permanent magnetic field perpendicular to an adjustable electric field. Only ions with a specific $\frac{q}{m}$ ratio can pass this filter. As neutral atoms are unaffected by this selection process, the beam path is tilted by 1.2° to ensure that neutrals do not pass the filter. Secondly, electronic lenses and deflection plates are employed to shape the beam consisting of the filtered ions. This process is crucial for achieving uniform irradiation within the desired target area.

After shaping the beam, it enters the experimental chamber containing the target mounted on the QCM target holder. During the experimental campaign, a quadrupole mass spectrometer (QMS) was installed in the experimental chamber. The necessity for its installation will be discussed in chapter 5. Figure 9 shows the overall experimental setup that was described previously.

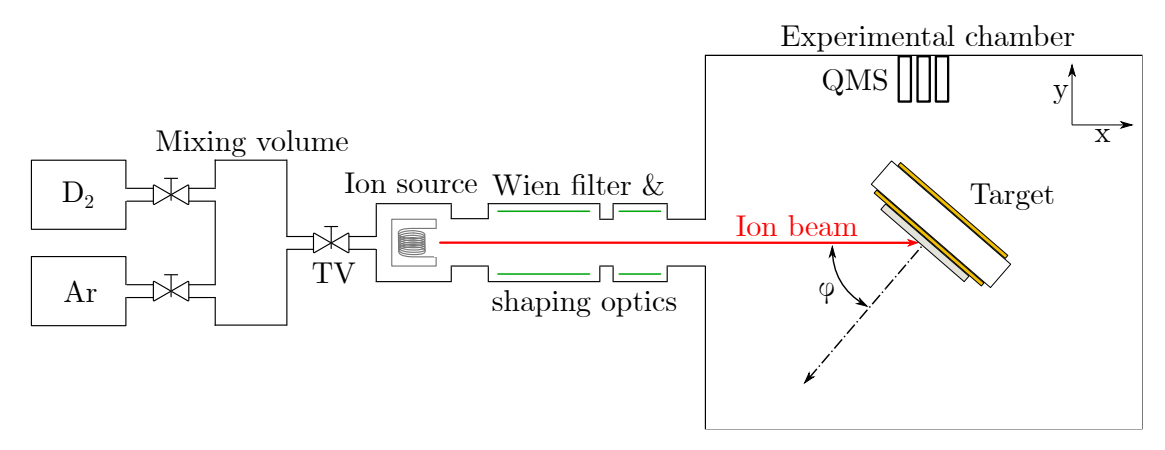


Figure 9: Schematic of the QSPARX experimental setup. Taken and adapted from [18].

The QCM target holder consists of several components. The most important feature is the QCM itself, which was described in more detail in section 2.1. In addition, a Faraday Cup (FC) is installed on the QCM target holder to enable current measurement. This is essential for the evaluation of the ion beam intensity and shape. Furthermore, the target holder can be heated to a specific temperature by ohmic heating. The temperature can be measured via a thermocouple that is mounted close to the QCM sample. This was particularly important for measurements with D_2^+ ions, which will be further discussed in chapter 5. The holder itself is mounted on a manipulator, allowing movement in all spatial directions and rotation along the manipulator axis, indicated by the angle φ in Figure 9.

As mentioned in section 2.1 the quartz is performing shear mode oscillations at its resonance frequency ($\approx 6 \,\mathrm{MHz}$). In this oscillation mode, changes of the frequency can be translated to mass changes, which is exploited to calculate sputter yields.

The quartz is an element of a circuit and it has been observed that by exciting the crystal to oscillate, the total circuit exhibits an impedance minimum at the resonance frequency of the circuit. Dedicated electronics, which are summarized in a so-called phase box and were developed previously at IAP [22] [28], then convert the oscillation property of the system into an analogue voltage signal that is designed to be zero at the impedance minimum. This voltage signal can then be converted via an analog-to-digital converter (ADC) to be read by a measurement computer. A proportional-integral-derivative (PID) controller is then used to control the frequency, while it may change over time, via a Tektronix AFG31000 function generator. More information on the control procedure can be found in [29]. A visualization of the control loop can be viewed in Figure 10.

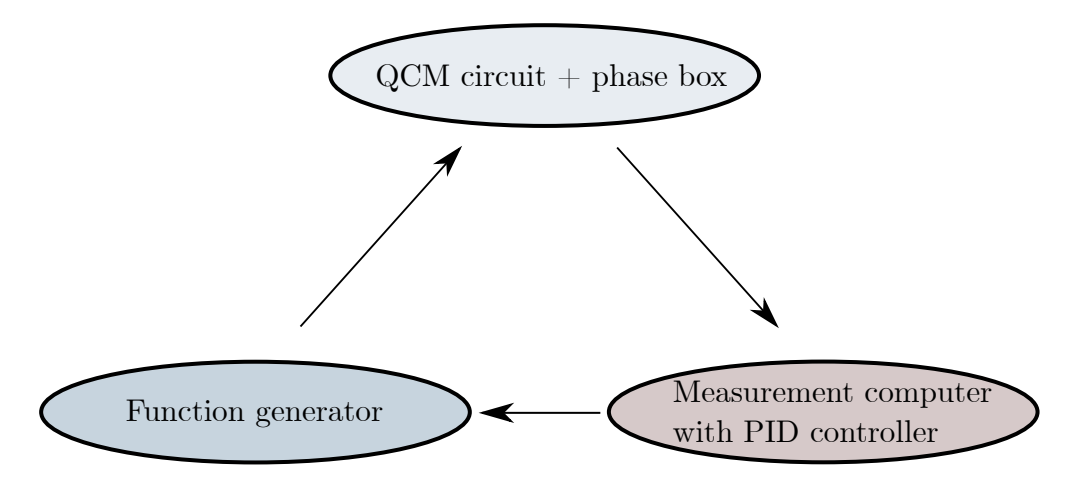


Figure 10: Visualization of the QCM control loop.

With this regulation of the drive frequency of the quartz, sputter yield measurements can be conducted. A general measurement procedure was established in the past and is introduced in the following section.

Measurement procedure

This section provides an explanation of the measurement procedure used during the course of this study, which was designed with the objective of enhancing the reproducibility of the resulting data. It is assumed that adequate vacuum conditions have already been established prior to the measurement process.

1. Beamprofile

In order to conduct the measurements, it is necessary to irradiate the sensitive area of the quartz uniformly. For this purpose, a $5 \times 5 \,\mathrm{mm}$ scanning was selected for the beam, which is sufficient to cover the quartz sensitive area, as previously described in more detail in section 2.1. The QCM target holder introduced in section 3.1 has a Faraday Cup installed that can be used to evaluate the shape of the beam by measuring a beamprofile. The profile is evaluated by measuring the current of the beam along two perpendicular lines in y and z direction (see Figure 9) that traverse the beam center. The center of the beam can be adjusted by the shaping optics parameters at 0×0 mm scanning. The shaping optics parameters have to be adjusted if the beam is not uniform enough and the new shape has to be evaluated. In this work, fluxes of $\approx 2 \cdot 10^{16} \frac{\text{ions}}{\text{m}^2 \text{s}}$ were reached. An example beamprofile can be seen in Figure 11.

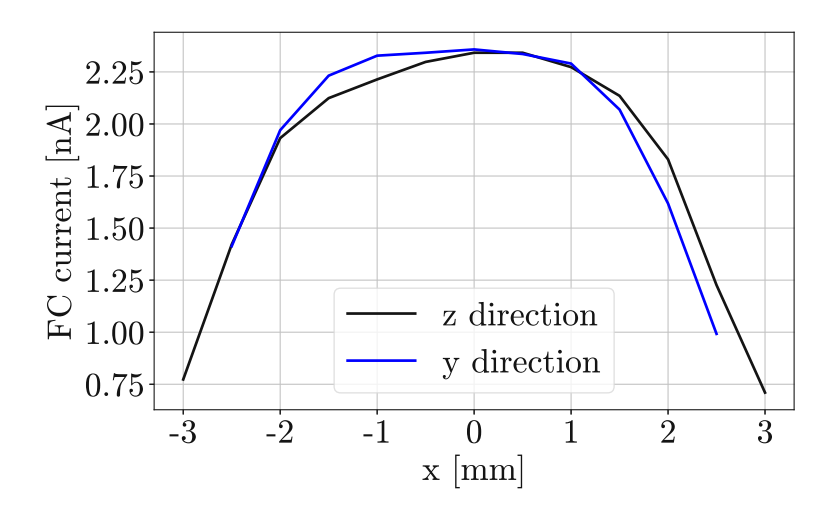


Figure 11: An example beamprofile recorded at the QSPARX. The measured FC current is plotted against the distance from the center of the beam, which is marked as 0.

2. Reaching steady state conditions

As soon as the shape of the beam is homogeneous in the desired area, one can irradiate the target. Prior to each measurement, the target is irradiated until a steady state yield is reached. This is done for several reasons. First, adsorbates tend to adhere to the surface of the sample and must be removed. Second, implantation plays an important role in irradiation experiments, with beam atoms implanted around a certain depth in the material. This increases the mass of the target. This would consequently introduce an error if one calculated the sputter yield at this point as the QCM can only measure absolute mass changes. Concurrently, the surface undergoes erosion by the incoming ions. In this picture, the implanted atoms move with a constant erosion velocity v_e towards the surface. A steady state is reached, when the implanted atoms reach the surface and therefore the material composition in the implantation range does not change further. At this point, mass changes are only induced by sputtering.

It was observed that the duration of this step varied depending on the projectile ions and the target material. D_2^+ ions require a substantially longer time than Ar⁺ ions to saturate due to the larger penetration depth of D₂⁺ compared to Ar⁺ at the same energy. Furthermore, the duration of this step increases with rising boron concentration in the target.

3. Angle sweeps

Once steady state conditions are met, the actual sputter yield measurements can be started. It starts with a beamprofile directly before the first angle measurement. After the completion of the beamprofile, the beam is deflected by changing the voltage in the Wien filter. Subsequently, the QCM target holder is moved to a position where the quartz can be irradiated. Angles between 0° and 70° are then measured. It was observed during the measurement campaign that angles up to 75° are feasible and consequently subsequent measurements were conducted to include irradiation at this angle. At each angle step the target is irradiated for a designated time, which is dependent on the specific sample and projectile. Between each angle step, the beam is briefly deflected until the next desired target position is reached. Additionally, time buffers of 50/100 seconds before/after motor movement are incorporated to ensure that vibrations from the movement do not influence the measurement. The angle sweeps are predominantly conducted automatically via a python script. However, in the case of the pure boron sample, they were performed manually. This was done due to the challenging nature of measuring sputter yields of samples with high boron content. This will further be discussed in chapter 5.

4. Beamprofile

The measurement is finished by taking a beamprofile directly after the final angle step. Therefore, the beam is deflected, and the QCM target holder is driven to the FC position. Subsequent to redirecting the beam at the FC, a beamprofile is taken to ascertain whether the beam intensity or shape has undergone significant change, or whether it can be assumed that it was constant throughout the measurement.

3.3 Data post-processing

Following the conclusion of the measurement process, the calculation of sputter yields is possible. However, it may be necessary to undertake post-processing of the data for a number of reasons, which are listed below.

1. Exponential trend to steady state yield

During the measurement campaign it was observed that sputter yields converge exponentially towards a steady state value for each angle. This is not surprising as the mean implantation depth is dependent on the angle of incidence of the projectile and therefore a new equilibrium state has to be reached for each angle. Consequently, the irradiation time per angle step has to be chosen so that a steady-state value can be reached within this time. The exponential tendency was observed to be more pronounced in samples with higher boron content, with the measurement of the pure boron sample requiring several hours per angle for 2 keVAr^+ irradiation. In comparison, tungsten samples require 230 seconds per angle step for Ar irradiation. Given that the layer thickness is only a few hundred nanometers, this introduces a new problem. It is not possible to irradiate the thin layer indefinitely, as this would result in the complete removal of the thin film over time. To circumvent this issue, exponential fits have been applied in order to extract the steady state yield for each angle step.

The exponential fits were conducted using the scipy library in Python [30]. As a fit function $f(x) = a \cdot \exp(bx) + c$ was used. The parameters a, b and c were fit parameters, with c representing the steady-state value in the procedure. The fits were applied to all of the measurement data from samples containing boron, if a fit was possible and the yield had not reached steadystate during the chosen irradiation time. If the yield had already reached its steady-state value, no fit was necessary. This was the case for measurements with the pure tungsten sample. The decision of whether a fit could be applied usefully or a steady state value had been found is at the discretion of



the experimenter. It was found that, in the case of measurements involving D_2^+ ions, the application of fits was not possible, except for individual data points in the measurement on pure boron. This is because the signal-to-noise ratio for 2 keV D₂⁺ irradiation is several orders of magnitude smaller than for 2 keV Ar⁺ irradiation. On the other hand, exponential fits to Ar⁺ measurement data could be applied in many cases. An example of such a fit for an angle step is depicted in Figure 12.

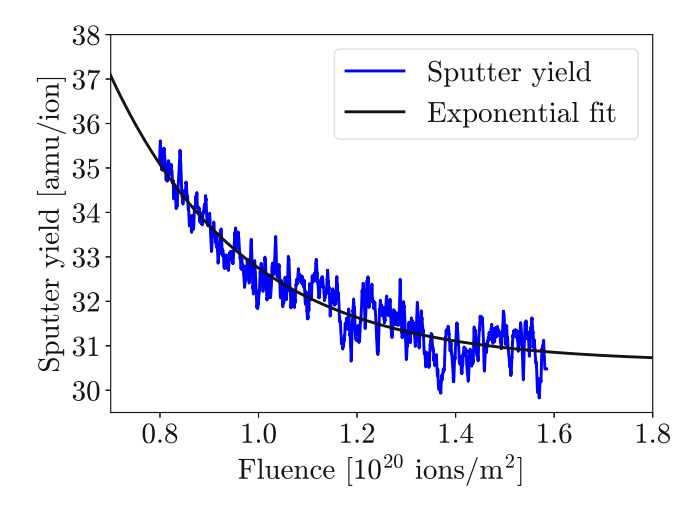


Figure 12: Exemplary case of a measured sputter yield as a function of the applied ion fluence with an exponential fit applied.

2. Temperature driven frequency drift

It has been demonstrated that the quartz eigenfrequency is subject to temperature dependent fluctuations [20]. Consequently, variations in temperature result in errors in the measurement. The main source for temperature changes was the change in laboratory room temperature, which relates directly to the QCM target holder temperature. The highest temperature difference that was observed during an angle step throughout all measurements was around $\Delta T = 0.3$ °C in the 2 keV Ar⁺ \rightarrow B measurement.

In the post-processing of the data points, thermal drift was addressed through the following procedure. As a first approximation, the frequency drift occurring before or after the irradiation was extracted from the frequency over time curve. Then, this value was subtracted from the frequency change that occurred during the bombardment. The resulting frequency change represents changes only induced by sputtering. To test this procedure, the method was preliminary applied for those data points in the $2 \,\mathrm{keV} \,\mathrm{Ar}^+ \to \mathrm{B}$ mea-



surement, where a linear trend of temperature change throughout the angle step could be assumed. As the resulting difference in yield was less than $1 \frac{\text{amu}}{\text{ion}}$ at the highest temperature change, this method is not applied in the post-processing at all. A further reason for not using this method is that immediately after irradiation, other effects such as outgassing or cooling due to the absence of the beam could interfere with the external temperature drift. Thus, it is not feasible to identify temperature-driven effects due to purely external influences via this procedure.

3.4 QMS

For some of the samples tested, additional experiments were carried out with a quadrupole mass spectrometer (QMS). It allows filtering of ionized residual gas atoms based on their mass to charge ratio by creating oscillating electric fields between four parallel metal rods [31]. The QMS was installed on a port, with a distance of a few 10 cm away from the target holder. The reason why a QMS was installed during the course of this project is given in section 5.2. The experiments conducted with the QMS had an identical procedure for the samples tested, which is described in the following.

At first, D_2^+ fluence was applied to the sample at room temperature. Following the application of sufficient fluence, the irradiation was stopped. After irradiation, it was necessary to wait for a certain time until the pressure in the experimental chamber fell below a threshold of 10^{-8} mbar. This procedure was implemented to prevent the recording of the gas utilized for irradiation as an element within the chamber by the QMS. Subsequently, the target holder was ohmically heated. The performed heatramp was initiated by a continuous increase of heating current from 0 until a maximum current I_{max} was reached. The ramp up was done in a specific time t_{ramp} . When I_{max} was reached, it was either held constant for a certain amount of time t_{hold} or a ramp down to $I_{\text{h}} = 0$ A within the time t_{ramp} began immediately. This whole procedure should be further addressed to as heatramp. Simultaneously, the occurrence of masses within the experimental chamber was detected by the QMS, thereby providing information on which elements were outgassing from the sample. This was achieved by continuously sweeping through a specified interval of atomic mass units (amu) at a specified measurement time per amu. The return value of the QMS was the measured ion current at a specific atomic mass unit. The magnitude of the current is directly proportional to the quantity of the measured element. In the data processing, an element was designated as detected if the value of the QMS ion current was positive for more than one cycle for a specific atomic mass unit. The experiments involving the QMS

were conducted subsequent to the sputter yield measurements for each compound sample.

3.5 AFM

An atomic force microscope is an important tool for analyzing surface structures in the nanometer region [32]. In this work, an AFM was utilized to identify the roughness of the produced layers and to observe any potential surface changes that could have occurred during irradiation. The microscope used in this study was an Asylum Research Cypher S operated under ambient conditions.

The AFM technique is based on the interaction of a tip with the surface atoms. The tip itself is mounted on a cantilever. A laser beam reflected from the cantilever is detected by a four-quadrant photodiode, allowing for precise height mapping while scanning over an area. The precise movement of the sample is controlled by a piezo stage. A schematic of the working principle can be seen in Figure 13.

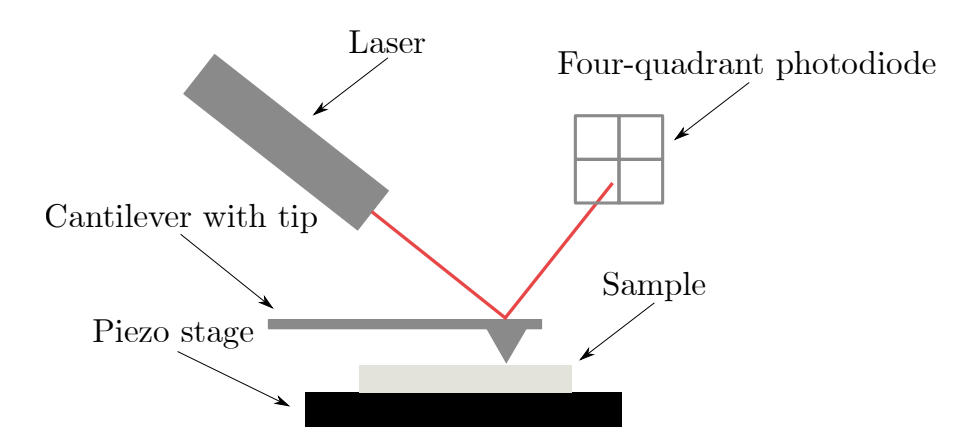


Figure 13: Visualization of the AFM measurement principle.

The interaction between the tip and the surface can be approximated by the Lennard-Jones potential, which describes the potential between neutral atoms. This potential can be divided into two regions. In one region, attractive forces such as van der Waals forces dominate and in the other region, repulsive forces such as Pauli repulsion are dominant. This can be exploited to operate the AFM in different modes.

In general, one can distinguish between static and dynamic operating modes. In dynamic modes, the cantilever is excited at a certain frequency. This is in contrast to the static mode, where the cantilever is not excited. Operation can be further



categorized as either contact or non-contact, referring to the relative position of the tip and surface. In this thesis, the dynamic tapping mode was utilized. This mode combines the contact and non-contact modes, as the tip is brought into contact with the surface and lifted off alternately. In tapping mode, the cantilever with a sharp tip is driven close to its resonance frequency. The force acting on the tip induced by the interaction with the surface changes the amplitude of the oscillation. A feedback loop is then used to maintain a constant amplitude by varying the height with the piezo stage, thus enabling imaging. The Lennard-Jones potential including the regions of the different operating modes can be seen in Figure 14. More information about AFM techniques can be found in [33] and [34].

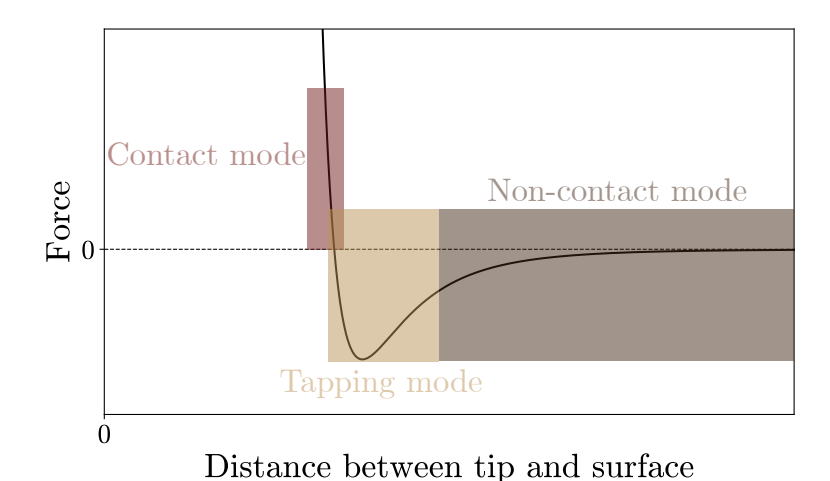


Figure 14: A visualization of the interaction potential between neutral atoms including associated AFM operation modes. The different regions are approximated from [35].

4 Sample characterization

In this study, a total of five samples was analyzed. The samples differed from each other in terms of the mixing ratio of tungsten to boron. The five samples comprised one pure tungsten sample, one pure boron sample and three compound samples (W:B ≈ 4.1 , W:B ≈ 1.1 , W:B ≈ 1.4). The thin tungsten/boron films were deposited via Radio Frequency (RF) magnetron sputtering at Uppsala University (UU) in Sweden on QCM quartzes provided by the company LapTech.

In RF magnetron sputtering, the target material (in this case tungsten and boron) is sputtered via a plasma and deposited on a substrate. The substrate usually used for further QCM measurements is a gold layer on top of the quartz (see Figure 7). The process of sputtering is induced by an alternating electric field, which prevents the target material from charging up on one hand and accelerates ions towards the target on the other. An additional magnetic field increases the deposition rate and prevents charged particles from etching the forming substrate. Detailed information on magnetron sputtering can be found in [36].

4.1 Sample compositions

Following production, an analysis of the sample compositions was conducted at UU using Time-of-Flight Elastic Recoil Detection Analysis (ToF-ERDA), which provides elemental depth resolution [37] [38] [39]. This is achieved by irradiating a target with heavy MeV ions such as iodine-127 and measuring the ion species and the energy of the recoils coming from the target. The concentration over depth distributions for the five samples can be seen in Figure 15. It is important to note that the samples investigated by means of this technique were twin samples of the actual samples employed in this thesis in order not to introduce any defects in the samples used for the sputtering studies. Since the twin samples were located directly next to each other during deposition of the layers, it is assumed that the composition of the produced layer is identical. As substrate for the samples used for analysis, a silicon wafer piece was chosen instead of the more fragile and valuable QCM substrate. The finite thickness of the layers produced can be clearly seen as the silicon increases in concentration after a few hundred 10^{15} atoms/cm². Elements designated as "other" in the graph represent impurities, such as hydrogen, deuterium, carbon, nitrogen, oxygen, fluor and argon. To enhance the clarity of the graphs, the precise depth distribution of individual impurities has been omitted and only the distribution of the sum of impurities is shown.

To obtain single concentration values suitable for the use in simulations, a mean value was calculated. The values in Table 4.1 represent the mean film composition at depths ranging from 200 to $600 \cdot 10^{15} \frac{\text{atoms}}{\text{cm}^2}$. This range is also highlighted in Figure 15. The same of the sam in Figure 15. Those values are taken as an input for the SDTrimSP simulations, which are compared to the experimental results in chapter 5.

	W	$^{10}\mathrm{B}$	$^{11}\mathrm{B}$	Η	D	\mathbf{C}	N	Ο	F	Ar	Si
Pure W											
W:B $\approx 4:1$	85.1	2.8	11.4	0.05	-	0.5	-	0.1	-	-	0.05
W:B $\approx 1:1$	55.6	8.5	34.3	0.1	-	0.9	-	0.1	-	-	0.5
W:B $\approx 1:4$	15.9	16.9	62.5	0.1	0.2	1.8	0.3	1	-	0.4	0.9
Pure B											

Table 4.1: Average sample compositions calculated from ToF-ERDA spectra in percent.

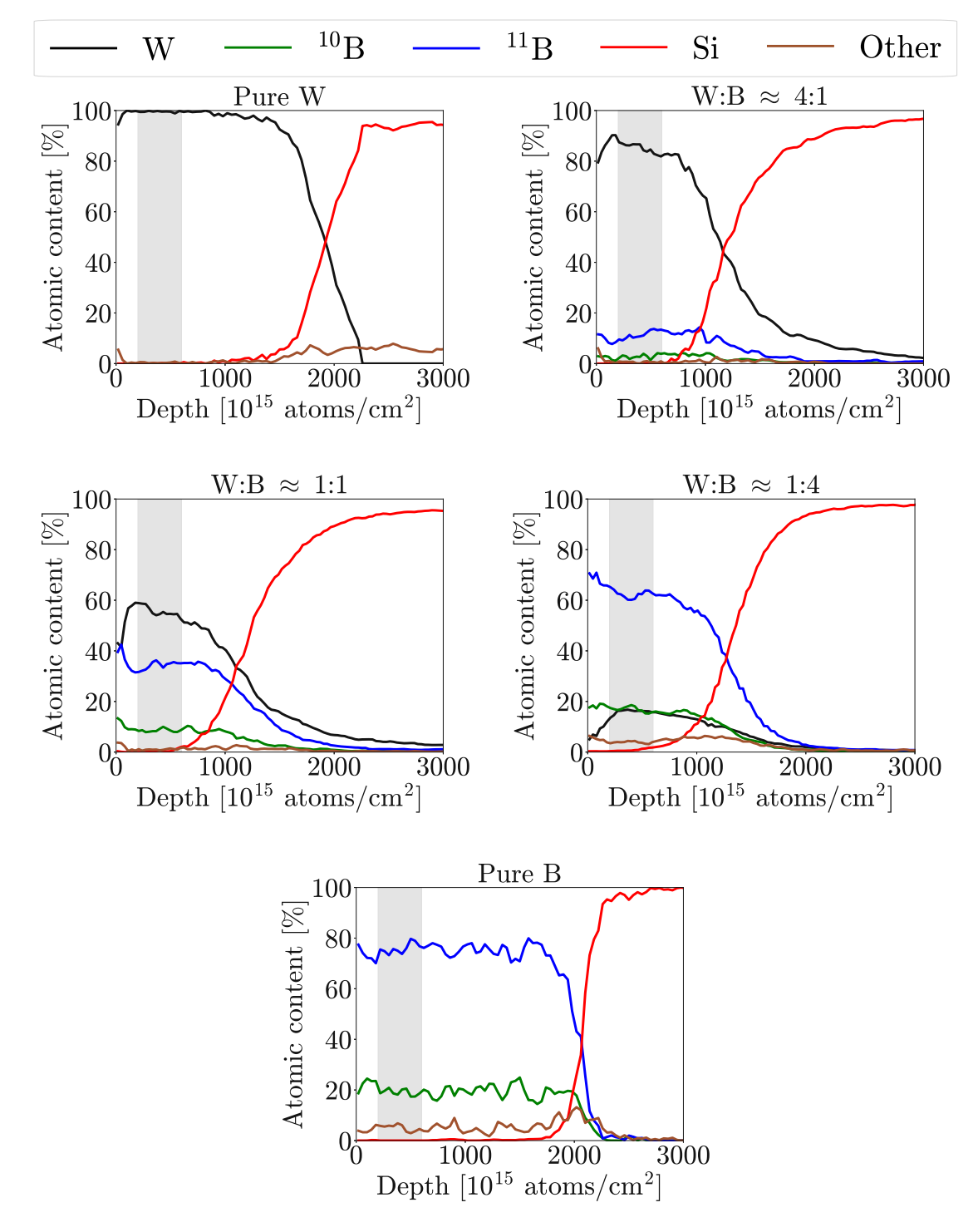


Figure 15: Concentration over depth values for the five investigated samples. The depth ranges taken for the calculation of the mean concentration values are marked in gray.

4.2 Surface properties

Surface properties such as the mean of the surface inclination angle distribution (SIAD) $\delta_{\rm m}$ and the root-mean-square roughness (RMS) $R_{\rm q}$ were extracted from AFM images. Images were taken from the center of the samples and from the edge before and after irradiation. The edge of the samples was not subjected to irradiation, as the beam did not reach this area. Consequently, a comparison can be made between irradiated and non-irradiated areas. The values for mean inclination angle and RMS roughness prior to irradiation are presented in Table 4.2. In order to achieve sufficient statistical validity, 1-3 images were taken per area. The mean values, along with their respective standard deviations, are shown. No drastic differences between edge and center values could be observed, indicating that the layers are homogeneous. The low roughness values and mean inclination angles confirm smooth, mirror-like surfaces.

	$R_{ m q}$	nm]	$\delta_{ m m}$ [6	deg]
	Center	Edge	Center	Edge
Pure W	2.18 ± 0.12	2.22 ± 0.04	8.14 ± 0.54	9.06 ± 0.15
W:B $\approx 4:1$	2.06 ± 0.01	2.17 ± 0.11	5.46 ± 0.06	5.88 ± 0.1
$W:B \approx 1:1$	1.6 ± 0.09	1.63 ± 0.05	4.9 ± 0.21	4.96 ± 0.01
W:B $\approx 1:4$	1.21	1.26 ± 0.03	3.59	3.83 ± 0.31
Pure B	1.73 ± 0.05	1.67	7.24 ± 0.14	7.82

Table 4.2: Surface properties before irradiation.

The AFM images themselves and the values after irradiation are shown in chapter 5 to have a direct comparison between pre- and post-irradiation behaviors.

Results and discussion

In this chapter, the experimental findings of this work are presented. However, before the first section, the general structure of this chapter is explained and information is given that is crucial for understanding the presented results.

Structure

Each section focuses on one particular sample, containing the results for the sputter yield, changes in surface properties and for the last three samples additional QMS experiments. The sections are arranged in the order the experiments were conducted. A comparison of the sputter yield between the samples is given in the final section.

Units of sputter yield

The unit of the y-axis of the sputter yield figures is always given in $\frac{\text{amu}}{\text{impinging ion}}$. It should be noted that this is actually the $\frac{\text{net mass removal}}{\text{impinging ion}}$ as this is the quantity the QCM can measure. The errorbars for the sputter yield measurements are due to fluctuations in the ion beam.

Eckstein fits

To the simulation data in section 5.1 - section 5.5, fits have been applied to guide the eye. These fits have been made with the Eckstein fomula

$$Y(\alpha) = Y_0 \cdot \left\{ \cos \left[\left(\frac{\alpha}{\alpha_0} \frac{\pi}{2} \right)^c \right] \right\}^{-f} \cdot \exp \left\{ b \left(1 - 1/\cos \left[\left(\frac{\alpha}{\alpha_0} \frac{\pi}{2} \right)^c \right] \right) \right\}$$
 (5.1)

which is a formula that is optimized for sputtering processes [40]. Y_0 represents the yield at 0° incidence angle, α the incidence angle, α_0 a parameter $\geq \frac{\pi}{2}$ and c, f, b are additional fit parameters. The fits were again performed using the scipy library in Python [30]. Yield over angle plots for the experimental data in subsection 5.6.1 also include Eckstein fits to guide the eye.

Simulation remarks

The simulations to which the experimental data is compared are dynamic SDTrimSP simulations. That means that the target composition is changed during the simulation. This approach is adopted to ensure improved comparability between the

simulation data and the experimental findings. The initial target composition used in the simulations is shown in Table 4.1 in section 4.1. The simulated yield in the figures is also given in $\frac{\text{net mass removal}}{\text{impinging ion}}$ to ensure comparability to the experimental yield.

In order to conduct the simulations, it is first necessary to select the relevant simulation input parameters. The interaction potential that was selected for this study was the Krypton-carbon (Kr-C) potential. This potential was chosen because it had been shown that the simulations agreed best to the experiments in most cases [25]. The integration method employed to calculate the scattering angle of a collision is Gauss-Legendre, which is the default method. For dynamic simulations, additional parameters can be selected to represent the transport of non-bound particles. These parameters are damage-driven diffusion η_0 and pressure-driven transport K_0 . The parameters have been introduced in the simulation code in order to achieve better agreement between simulation results and experimental data. The parameters represent the maximal concentration of the projectile that can be accumulated within the target. For the argon simulations, the values for these parameters have been taken from [25]. The values themselves are derived from experiments involving the irradiation of a silicon target with argon. However, no such parameters have been established for deuterium. After consultation with one of the authors of SDTrimSP, an initial guess for the diffusion parameters for deuterium was made so that the maximum concentration of deuterium is $\approx 40\%$ at 50 keV irradiation.

Experimentally, the $2 \text{ keV } D_2^+$ ions dissociate at the surface, resulting in two D particles carrying 1 keV kinetic energy each. In this picture, the dissociation energy of approximately 10 eV is neglected, which is reasonable when comparing it to the kinetic energy [41]. As SDTrimSP is unable to simulate the collision process with D_2 molecules, the simulations were conducted with 1 keV D atoms. To ensure comparability of the simulation results with experiments, the simulated yield coming from 1 keV D simulations was multiplied by a factor of two. The validity of this assumption has been verified in the past using molecular dynamics simulations [42].

AFM image comparison

When comparing surface properties extracted from AFM images, certain things need to be kept in mind. The AFM images themselves might depend on the used tip. The image actually represent a convolution of the tip morphology and the sample morphology. The comparability between individual AFM images can therefore be limited when different tips are used. Therefore, it was ensured that the same tip was used for edge and center imaging of the investigated samples

during the course of this study. However, it was not possible to use the same tip for the pre- and post-irradiation AFM images. This is because the time between the two measurements was too long and other images had been taken in the meantime. Therefore, a direct comparison can be made between the center and edge images. However, caution is advised when directly comparing images from before and after irradiation.

5.1 Pure tungsten

The pure tungsten sample was the first sample tested in order to have comparable data with the past and to check the functionality of the experimental setup.

5.1.1 Sputter yield

Figure 16 shows the experimentally obtained sputter yield compared with past data from [18] [19] [43]. In the left part of the figure the experimental yield is shown for 2 keV Ar^+ irradiation and in the right part the same for 2 keV D_2^+ irradiation. Very good agreement can be seen. Figure 17 shows the results of the irradiation of the pure tungsten sample. In the left part of the figure the experimental yield is shown along with four different simulations for 2 keV Ar⁺ irradiation and in the right part the same for $2 \text{ keV } D_2^+$ irradiation. The experimental points were obtained by measuring in a random order for both argon and deuterium irradiation with the general measurement procedure explained in section 3.2. The beamtime per angle step was 230 s for the argon measurement and 3000 s for deuterium.

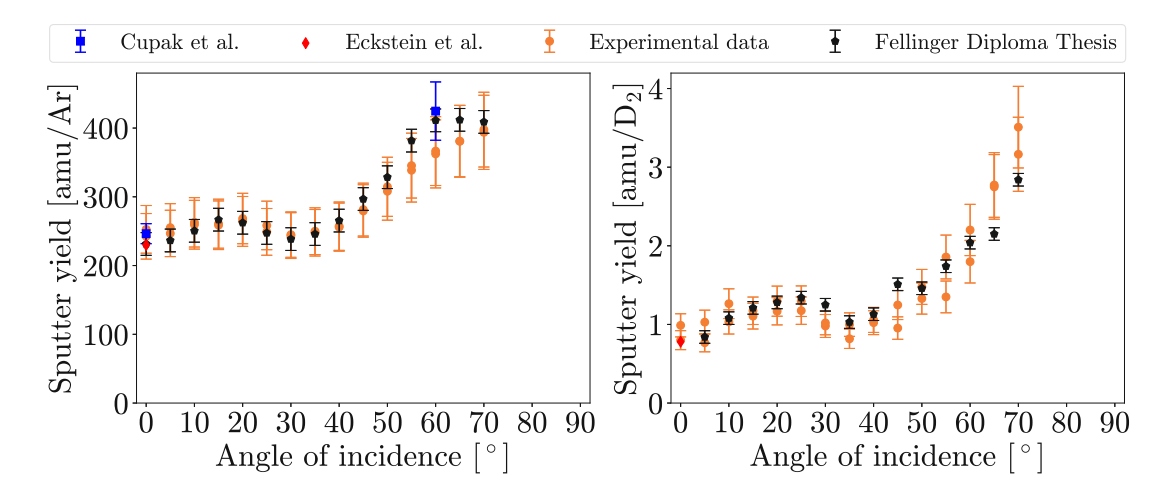


Figure 16: Experimental sputter yield of the pure tungsten sample irradiated with 2 keV Ar^+ ions at the left and 2 keV D_2^+ ions at the right compared with data from [18] [19] [43].

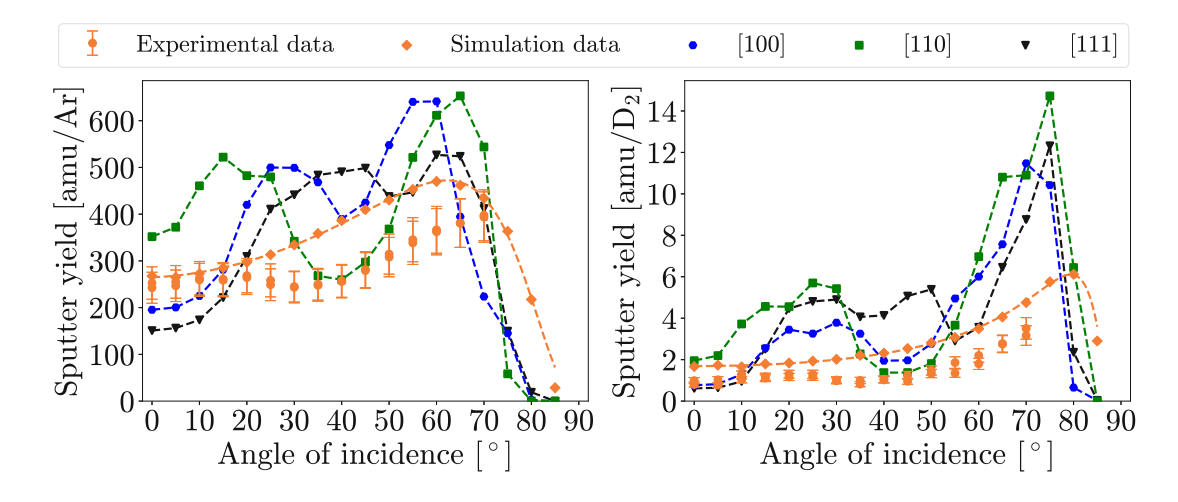


Figure 17: Experimental sputter yield of the pure tungsten sample irradiated with 2 keV Ar^+ ions at the left and 2 keV D_2^+ ions at the right compared with simulations from SDTrimSP. Additionally to a dynamic amorphous target simulation, static crystalline structures with indicated crystal orientation are shown in the plots.

As was the case with previously obtained measurements, the yield over angle curve of pure tungsten showed a minimum at approximately 30° for argon and 35° for deuterium measurements [18]. Previous data suggest that the dip is due to a texture effect which is a direct consequence of the presence of a predominant crystallographic orientation on the surface [44]. The most recent version of the SDTrimSP software permits the selection of both amorphous and crystalline targets, which allows to further investigate the suggested texture effect. Given that tungsten forms a body-centered cubic (bcc) crystal, it is possible to identify a crystal orientation that fits best to the experimental data. Initially, three orientations were tested in addition to the dynamic amorphous simulation. It is important to note that the crystal simulations were conducted in static mode, where the target composition remains constant and no amorphization occurs. The position of the dip suggests that the simulation using the [110] direction agrees best with the experimental data. However, the alignment is not perfect, indicating that the sample does not correspond to a pure [110] crystal. It is more probable that the crystal is a mixture of different crystal orientations or amorphous structures with a predominant [110] direction. This could also explain the quantitative offset between simulated and experimental data visible in Figure 17, at least for some data points. To this sample a total fluence of $\approx 1.3 \cdot 10^{20} \frac{Ar^+}{m^2}$ and $\approx 6 \cdot 10^{21} \frac{D_2^+}{m^2}$ was applied.

5.1.2 Surface changes

In Table 5.1 AFM images for the pure tungsten samples are shown. Table 5.2 shows the surface properties extracted from the AFM images before and after irradiation. One can see that the values for center and edge are very similar to each other looking at the pre-irradiation values and post-irradiation values separately. This indicates that no noticeable change of the surface has happened during the bombardment.

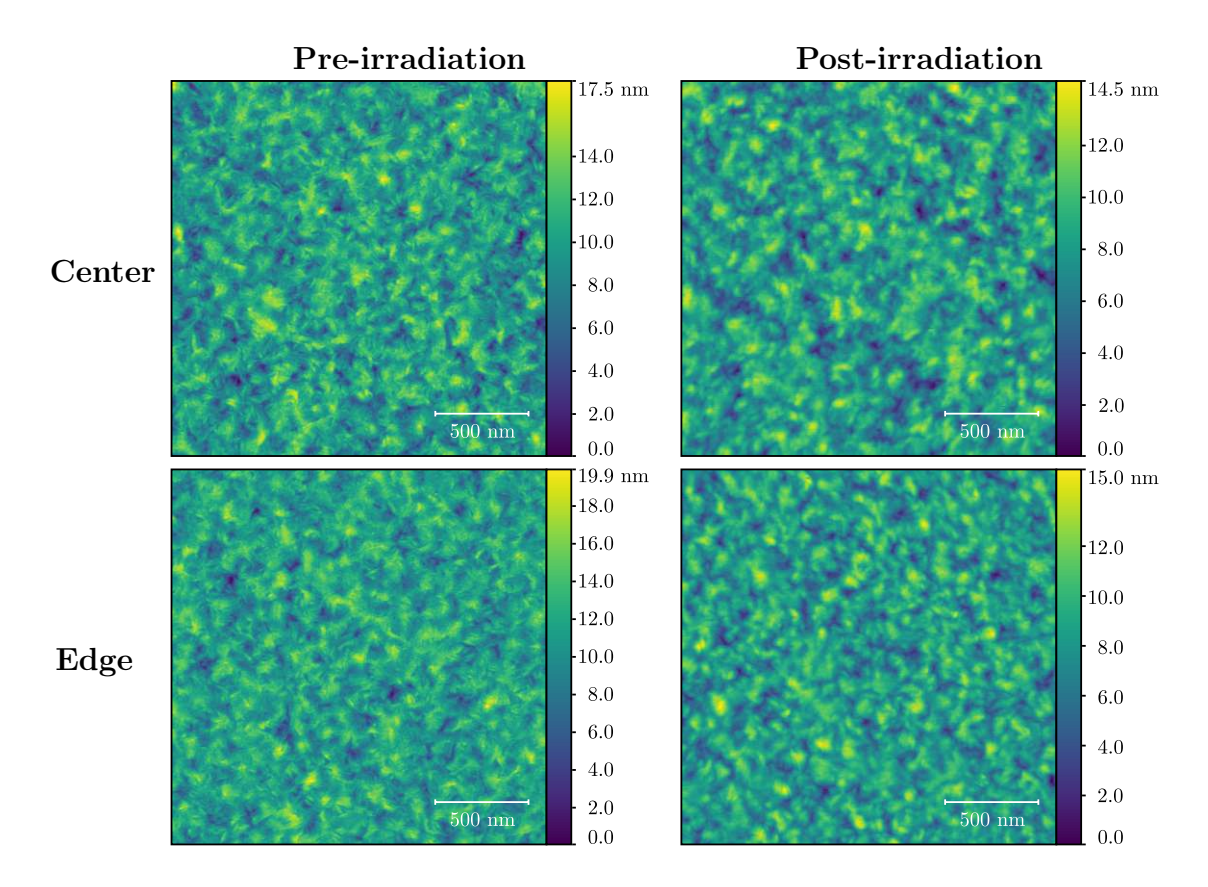


Table 5.1: AFM images for the pure tungsten sample before and after irradiation for irradiated area (center) and non-irradiated area (edge).

	Pre-irradiation	Post-irradiation
$R_{\rm q}$ center [nm]	2.18 ± 0.12	2.01 ± 0.05
$R_{\rm q}$ edge [nm]	2.22 ± 0.04	1.98 ± 0.06
$\delta_{\rm m}$ center [deg]	8.14 ± 0.54	6.31 ± 0.06
$\delta_{\rm m}$ edge [deg]	9.06 ± 0.15	6.34 ± 0.24

Table 5.2: Values for the RMS roughness and mean inclination angle before and after irradiation for the pure tungsten sample.

5.2 Pure boron

Measurements on boron containing samples were difficult to perform at first due to the lack of experience with this element. The pure boron sample was the first sample to be measured that was containing boron and as a consequence it required the most time to obtain satisfactory results.

5.2.1 Sputter yield

Argon measurements

As a first guess, the pure boron sample was treated similar to the pure tungsten sample. Therefore, the beamtime chosen for the first angle sweep was again 230 s in the argon case. However, the slope of the frequency curve was found to be negative for some angles, which can be seen in Figure 18. According to Equation 2.1, a negative frequency change is equal to a net mass gain. After additional measurements to ensure reproducibility, the experiments revealed that the angles at which a negative slope was detected occurred at low angles (0°-20°) and only if a high angle (50°-70°) had been measured previously, a phenomenon that is also evident in Figure 18. This effect, depending on the sample history, could be explained by taking into account implantation. At lower angles, the mean implantation depth of projectiles is larger than at higher angles. Consequently, it is plausible that projectiles reach a depth that is not yet saturated after a transition from a higher to a lower angle. This leads to a negative mass change or reduction in the measured yield. Additionally, outgassing from deeper layers is possible when measuring a higher angle directly after a lower one. It is important to note that these observations are not limited to boron and are applicable to other elements as well. However, it was observed that the time required for each angle step to reach a steady state is significantly longer for boron, which excludes the possibility of reaching a steady state within the originally selected time frame of 230 s.

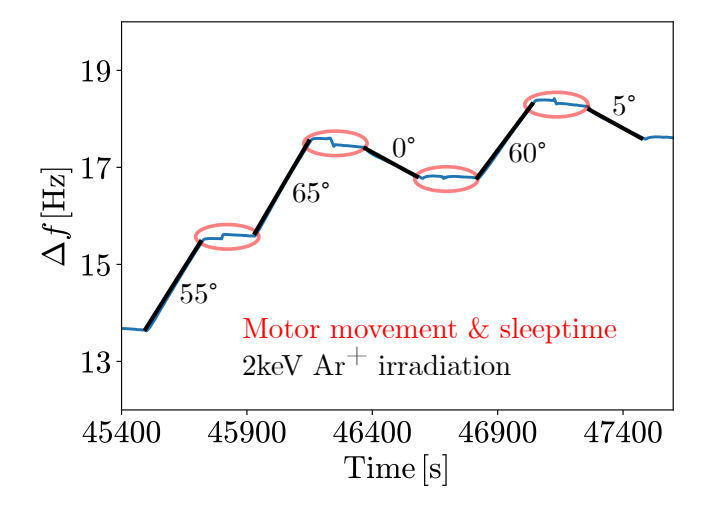


Figure 18: Part of the 2 keV Ar⁺ frequency curve during the measurement. Δf denotes the difference between the eigenfrequency f_0 at the measurement start and the frequency at a given time during the measurement.

In order to mitigate the effects of implantation and outgassing, it was decided to measure in ascending and descending order instead of approaching the angles in a random order. This ramp up and ramp down procedure was applied for the remaining experimental campaign. As the beamtime per angle step was also not obvious, all measured angles were conducted manually. Each angle was irradiated until a steady state yield could be determined. This resulted in different beamtimes for each measured point ranging from 2000s to 9050s. For higher angles, the required time was typically larger, as a lower flux is applied to the sensitive quartz area. The large irradiation times resulted in significant erosion of the boron layer. In order to avoid a complete erosion of the boron layer, it was necessary to exclude some angles from the measurement. The results for the argon measurement are provided in the left part of Figure 19. It can be seen that the experimental yield is slightly lower than the yield predicted by the simulation. Nevertheless, as the trend exhibited by both curves is identical, this suggests that the pure boron target was indeed amorphous. In total, a comparably high argon fluence of $\approx 2.7 \cdot 10^{21} \frac{\text{Ar}^+}{\text{m}^2}$ was applied.

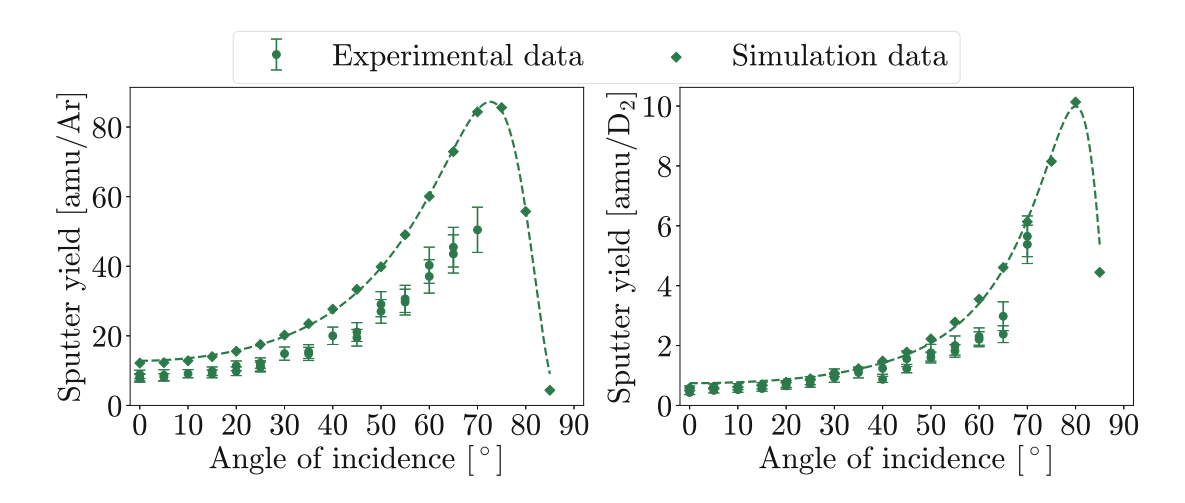


Figure 19: Experimental sputter yield of the pure boron sample irradiated with 2 keV Ar^+ ions at the left and 2 keV D_2^+ ions at the right compared with simulations from SDTrimSP.

Deuterium measurements

After the argon measurement, experiments with D_2^+ on pure boron at room temperature were conducted. However, even after applying fluences of $\approx 5 \cdot 10^{21} \frac{\rm ions}{\rm m^2}$ to the sample, a steady state could not be achieved. The sample continuously gained mass during D_2^+ bombardment, as indicated by the negative slope in the frequency curve in Figure 20. Some spikes can be seen in the frequency over time curve. These spikes can be attributed to short deflections of the beam for example to refill the gas volume.

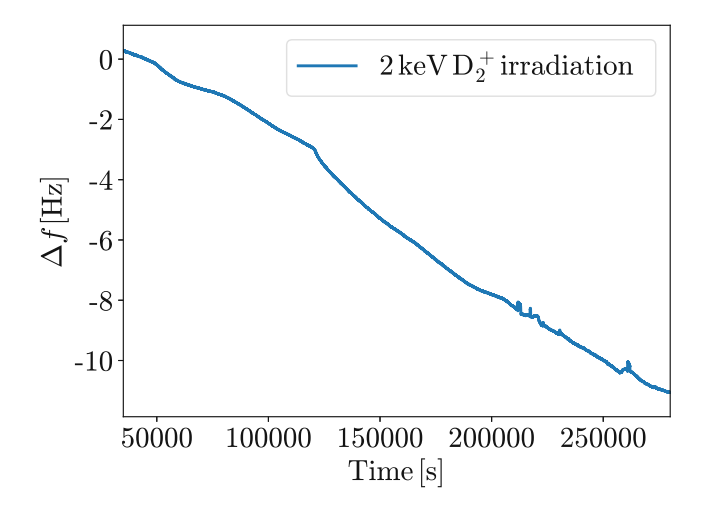


Figure 20: Part of the $2 \, \mathrm{keV} \, \mathrm{D}_2^+$ frequency curve during the measurement. Δf denotes the difference between the eigenfrequency f_0 at the start of the measurement and the present frequency at a given time.

One potential explanation for the observed mass gain might be attributed to the chemical binding of deuterium or residual oxygen to boron as it reaches the surface. Saturation of this effect could not be achieved experimentally within the applied fluence. In order to circumvent this steady mass increase, it was decided to repeat the measurement at elevated sample temperature with the exception that most adsorbed particles will desorb at such higher temperatures. Thus, the temperature at which the quartz frequency-temperature curve exhibited a minimum was selected for this purpose. This ensures that temperature fluctuations have minimal influence on the quartz frequency. The temperature recorded with the thermocouple was approximately 150°C with a heating current of $I_h = 1.82 \,\mathrm{A}$ through the heating wires of the target holder. At this elevated temperature, a steady state could be achieved and sputter yield measurements could be conducted. These measurements were conducted automatically with a chosen beamtime of 7200 s. The results can be seen on the right side of Figure 19. Good agreement between

experiment and simulation is observed up to 35°. However, from 40° to 65°, a divergence emerges between the simulation and experiment, though they overlap again within the errorbars at 70° incident angle. The underlying reason for this behavior remains unclear and requires further investigation. The experimental curve displays no texture-related dips, thus indicating the presence of an amorphous structure. In total, a fluence of $\approx 1.2 \cdot 10^{22} \frac{D_2^+}{m^2}$ was applied during the deuterium measurement to this sample.

In order to investigate the possible binding and remission of deuterium to the boron sample, a QMS was installed after the completion of experiments with pure boron. Additional tests were conducted on all subsequent samples using the QMS, which are explained in the respective subsections.

5.2.2 Surface changes

Table 5.3 and Table 5.4 show the AFM images and the extracted surface properties. It can be seen that in this case a change in properties occurred comparing irradiated and non-irradiated area. The values of $R_{\rm q}$ and $\delta_{\rm m}$ are both found to be significantly lower in the irradiated area compared to the non-irradiated. This observation indicates that the surface underwent a smoothing process during the bombardment. However, also the non-irradiated area shows a slight decrease in $R_{\rm q}$ and $\delta_{\rm m}$, which could be attributed to the different tip that was used.

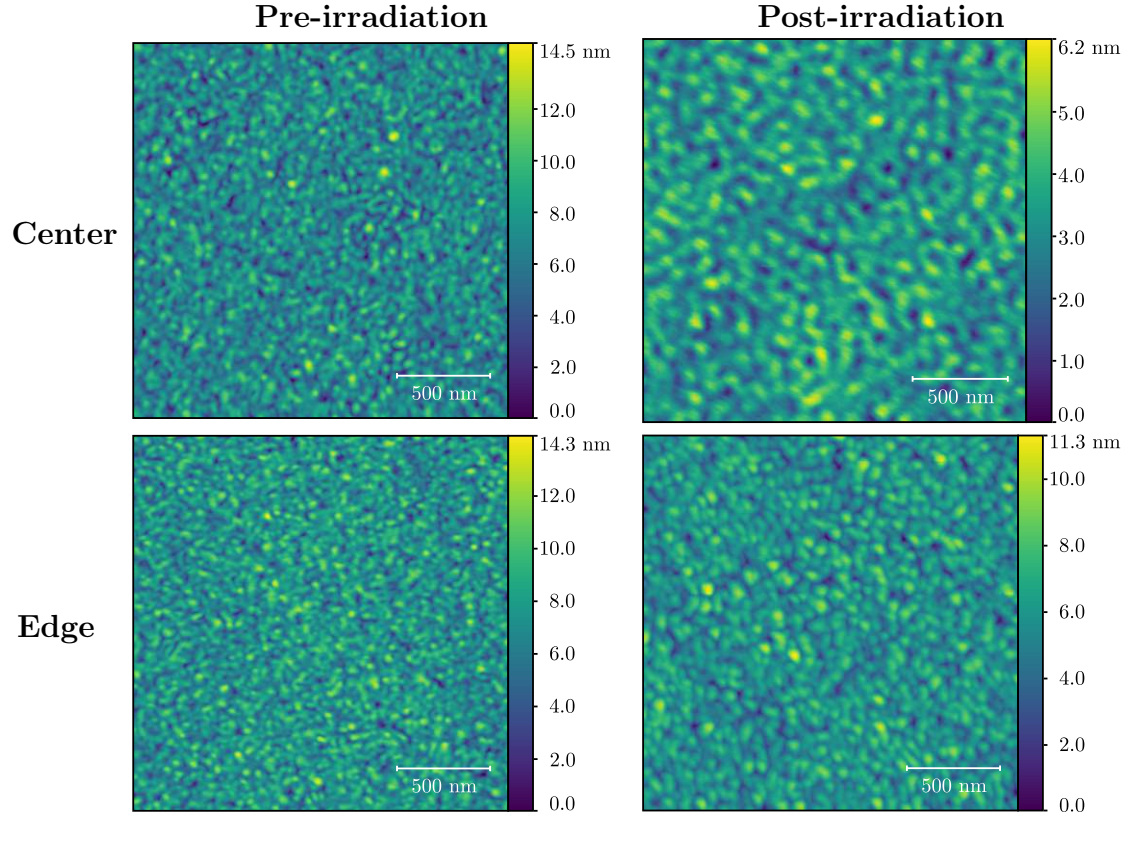


Table 5.3: AFM images for the pure boron sample before and after irradiation for irradiated area (center) and non-irradiated area (edge).

	Pre-irradiation	Post-irradiation
$R_{\rm q}$ center [nm]	1.73 ± 0.05	0.89 ± 0.05
$R_{\rm q}$ edge [nm]	1.67	1.27 ± 0.06
$\delta_{\rm m}$ center [deg]	7.24 ± 0.14	2.56 ± 0.13
$\delta_{\rm m}$ edge [deg]	7.82	4.9 ± 0.51

Table 5.4: Values for the RMS roughness and mean inclination angle before and after irradiation for the pure boron sample.

$5.3 \text{ W:B} \approx 1:1$

The first compound sample that was investigated was the W:B ≈ 1.1 sample. As previously mentioned, the angle sweeps were conducted in a ramp-up and rampdown manner in order to minimize the effects of implantation and outgassing. Furthermore, it was tested whether irradiation at an angle of 75° is feasible. Since it was found that approaching this angle is possible, the angle was incorporated



into the measurement procedures for all subsequent experiments. Furthermore, measurements involving the QMS were conducted after completing the sputter yield measurements for both ion types.

5.3.1 Sputter yield

In order to achieve a steady state yield, a beamtime per angle step of 900s for the argon measurement and 7200s for deuterium was chosen. For measurements with D_2 , the target was again heated with a heating current of $I_h = 1.82 \,\mathrm{A}$. A temperature of approximately 144°C was recorded with the thermocouple at this specified current. It was observed that the same current did not result in the same temperatures of the target holder. Several reasons for this can be identified. During the exchange of samples, the experimenter is required to unscrew and rescrew both the thermocouple and the heating wires from the target holder. It is possible that the connection of the thermocouple to the target holder was not identical before the sample was changed. The same possibility could apply to the heating wires. This could potentially lead to a change in resistance, which in turn would result in a variation in heating power. Another potential contributing factor could be the deterioration of the heating filament itself. Still a final answer could not yet been found.

The results for the 2 keV Ar⁺ irradiation are displayed on the left side of Figure 21, whereas the results for the $2 \text{ keV } D_2^+$ irradiation are displayed on the right.

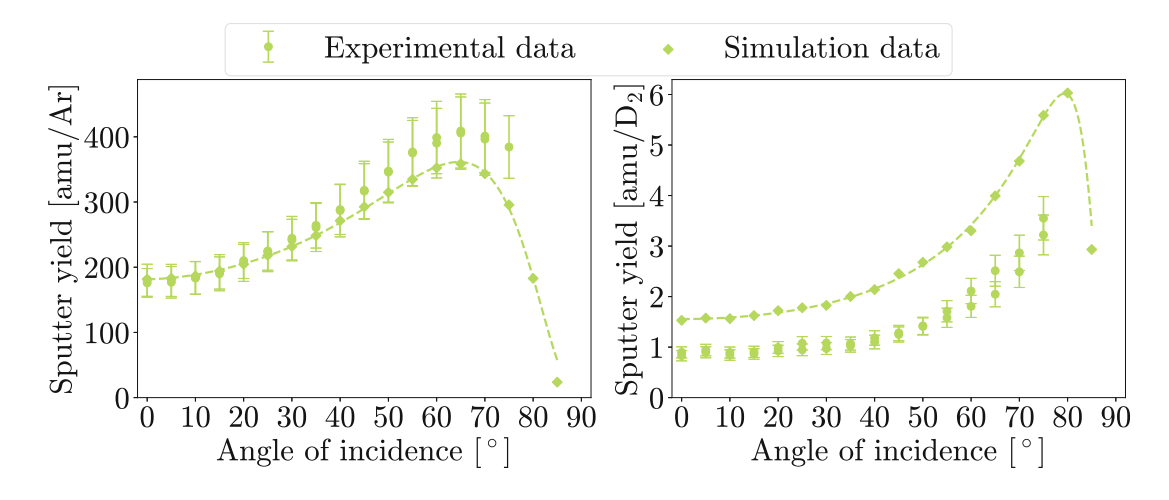


Figure 21: Experimental sputter yield of the W:B \approx 1:1 sample irradiated with 2 keV Ar^+ ions at the left and 2 keV D_2^+ ions at the right compared with SDTrimSP simulations.

Good agreement between simulation and experimental data can be seen in the argon case. However, a clear offset between experiment and simulation is evident in the deuterium case. Nevertheless, results indicate an amorphous target structure. To this sample fluences of $\approx 6 \cdot 10^{20} \frac{\text{Ar}^+}{\text{m}^2}$ and $\approx 6.2 \cdot 10^{21} \frac{\text{D}_2^+}{\text{m}^2}$ have been applied in total. This is roughly half the fluence that was applied to the pure boron sample.

5.3.2 Surface changes

Table 5.5 and Table 5.6 show the AFM images and the respective values for $R_{\rm q}$ and $\delta_{\rm m}$. A slight change in roughness and mean inclination angle is observable when comparing irradiated and non-irradiated areas. The irradiated area once again appears to have undergone a smoothing process. However, the values overlap within the standard deviation, and therefore this change could also be attributed to statistical fluctuations.

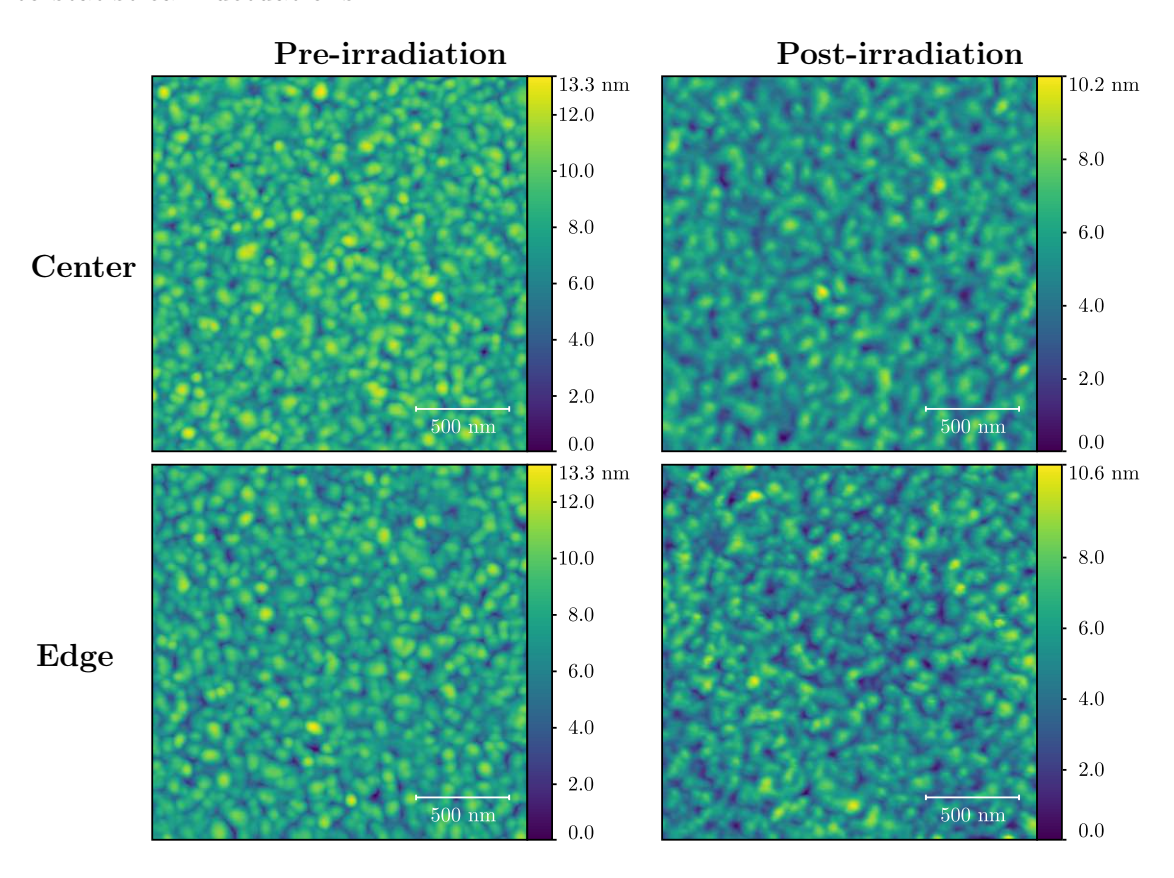


Table 5.5: AFM images for the W:B \approx 1:1 sample before and after irradiation for irradiated area (center) and non-irradiated area (edge).

	Pre-irradiation	Post-irradiation
$R_{\rm q}$ center [nm]	1.61 ± 0.09	1.32 ± 0.09
$R_{\rm q}$ edge [nm]	1.63 ± 0.05	1.53 ± 0.14
$\delta_{\rm m}$ center [deg]	4.9 ± 0.21	3.63 ± 0.52
$\delta_{\rm m}$ edge [deg]	4.96 ± 0.01	4.42 ± 0.54

Table 5.6: Values for the RMS roughness and mean inclination angle before and after irradiation for the W:B \approx 1:1 sample.

5.3.3 QMS measurements

In order to investigate the possible binding of deuterium to boron, as suggested by the measurement of the pure boron sample, the residual gas during a heatramp was analysis via the QMS. At first, a fluence of $\approx 7.8 \cdot 10^{20} \frac{D_2^+}{m^2}$ was applied to the sample at ≈ 35 °C. This was not room temperature, as the filament of the QMS was already running during irradiation and it heated the target holder from 27°C to approximately 35°C. After waiting for approximately 8 hours for the pressure to drop, a heatramp was started. A maximal heating current of $I_{\text{max}} = 1.82 \,\text{A}$ was reached over a period of 7 hours. This resulted in a maximal temperature of approximately 141°C. However, this was not the 144°C that had been measured previously at this current. This was due to the decrease in heating current beginning instantly after reaching its maximum $(t_{\text{hold}} = 0)$ and the target holder not yet being in thermal equilibrium. This was done as a first guess, but all subsequent heatramps are conducted with $t_{\text{hold}} = 1 \,\text{h}$. For this first heatramp a scanning interval of 0-50 amu and a measurement time of $200 \frac{\text{ms}}{\text{amu}}$ were chosen. However, no elements were recorded within this heatramp.

After completion of the first heatramp, another one was conducted without additional irradiation. It was conducted with $t_{\text{ramp}} = 7 \,\text{h}$, $t_{\text{hold}} = 1 \,\text{h}$ and a higher maximal heating current $I_{\text{max}} = 2.5 \,\text{A}$. To detect possible heavier elements, a bigger scanning interval of $0-200\,\mathrm{amu}$ and a measurement time of $200\,\mathrm{\frac{ms}{amu}}$ were chosen. It resulted in a maximal temperature of approximately 205°C. For this heatramp the only identifiable mass was 18 amu, most likely corresponding to water (H_2O) . It is likely that the water originates not from the sample itself, but from residual water on the target holder that evaporated during the heatramp. The detected ion current of the QMS over temperature can be seen in Figure 22.



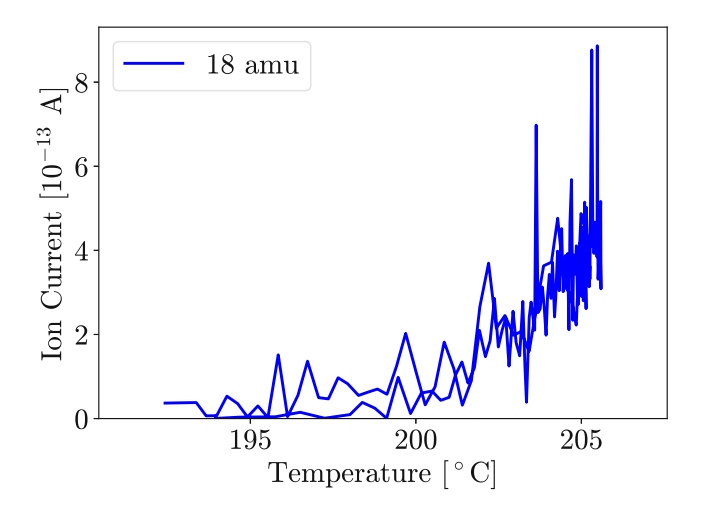


Figure 22: The QMS ion current plotted over the temperature during the heatramp. The only detectable element had mass number 18, most likely corresponding to H_2O .

No other elements were detected within this heatramp. This is surprising as outgassing from implanted deuterium was expected. One potential explanation could be that the deuterium had outgassed already during the first heatramp, but the outgassing rate was below the detection limit of the QMS.

$5.4 \text{ W:B} \approx 4:1$

5.4.1 Sputter yield

For this sample a beamtime of 1200s was chosen for the argon irradiation and 5400 s was chosen for the deuterium irradiation. Once more, a heating current of $I_h = 1.82 \,\mathrm{A}$ was chosen. It was again found that the recorded temperature of 104°C does not agree with previous measurements at the same heating current. The results for the sputter yield measurements can be seen in Figure 23. The left side shows the sputter yield during argon bombardment in $\frac{amu}{Ar}$, whereas the right side displays it for the case of deuterium irradiation in $\frac{amu}{D_2}$.

Almost perfect agreement between experiment and simulation can be observed for the argon case. Even though the trend of the curve is equal, the deuterium measurement again shows an offset, as the experimental data is lower than the simulation data. The experimental data in both cases again suggests amorphous target structure. A total fluence of $\approx 9.6 \cdot 10^{20} \frac{Ar^+}{m^2}$ and $\approx 5.1 \cdot 10^{21} \frac{D_2^+}{m^2}$ was applied.

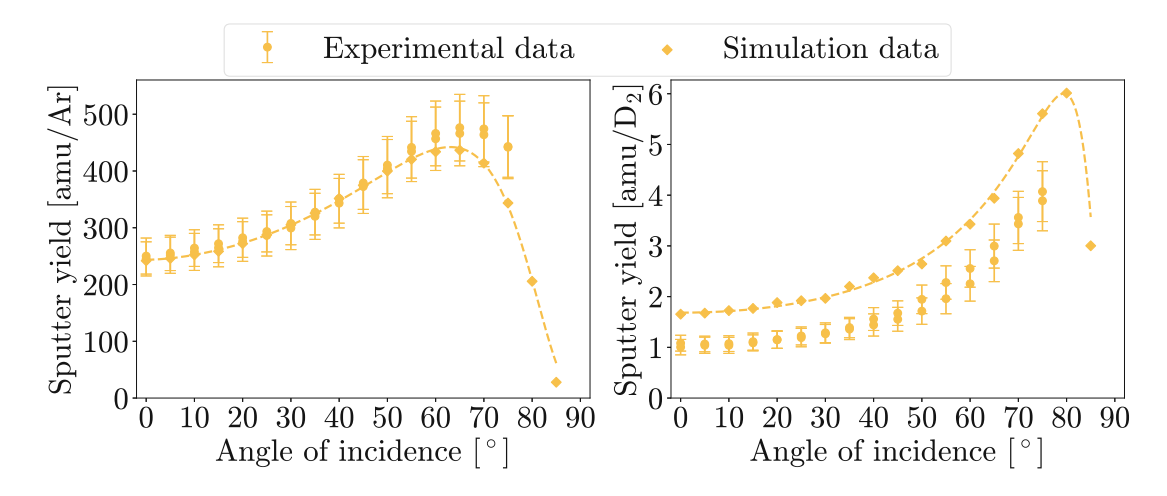


Figure 23: Experimental sputter yield of the W:B ≈ 4.1 sample irradiated with 2 keV Ar^+ ions at the left and 2 keV D_2^+ ions at the right compared with SDTrimSP simulations.

5.4.2 Surface changes

In Table 5.7 and Table 5.8 the AFM images themselves and the corresponding RMS roughness values and mean inclination angles are presented. It can be seen that there is a difference of $R_{\rm q}$ and $\delta_{\rm m}$ between images on the edge and the center. This observation indicates that the surface had undergone a transformation during the irradiation process. The surface appeared to be rougher after the bombardment. This phenomenon could possibly be attributed to preferential sputtering. However, this hypothesis would require further validation, for example through the utilization of ToF-ERDA measurements.

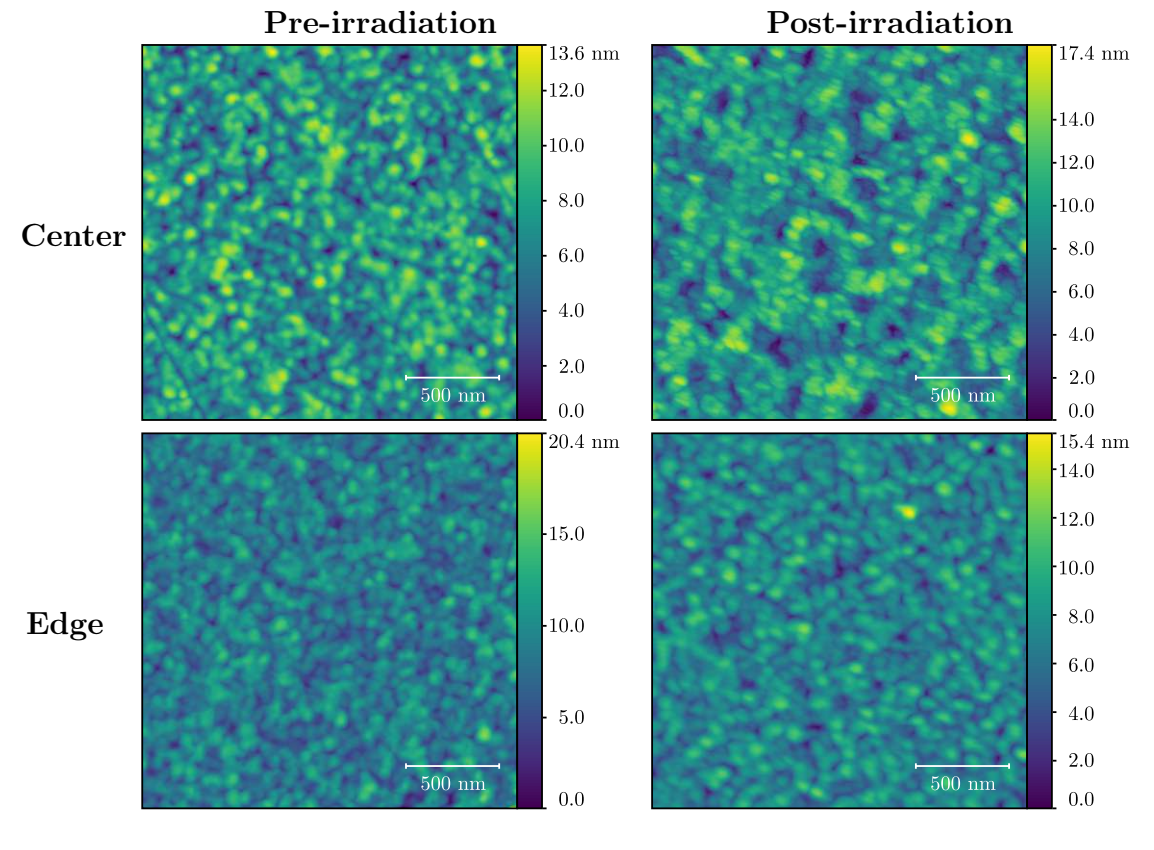


Table 5.7: AFM images for the W:B \approx 4:1 sample before and after irradiation for irradiated area (center) and non-irradiated area (edge).

	Pre-irradiation	Post-irradiation
$R_{\rm q}$ center [nm]	2.06 ± 0.01	2.61 ± 0.01
$R_{\rm q}$ edge [nm]	2.17 ± 0.11	1.69 ± 0.03
$\delta_{\rm m}$ center [deg]	5.46 ± 0.06	6.63 ± 0.42
$\delta_{\rm m}$ edge [deg]	5.88 ± 0.1	4.68 ± 0.25

Table 5.8: Values for the RMS roughness and mean inclination angle before and after irradiation for the W:B \approx 4:1 sample.

5.4.3 QMS measurements

First, a fluence of $1.1 \cdot 10^{21} \frac{D_2^+}{m^2}$ was applied to the sample at room temperature. Subsequent to the pressure dropping below 10^{-8} mbar a heatramp was initiated, with the parameters set to $t_{\text{ramp}} = 6 \,\text{h}$, $t_{\text{hold}} = 1 \,\text{h}$ and $I_{\text{max}} = 3 \,\text{A}$. A higher current then previously was selected because the temperature at $I_{\rm h}=1.82\,{\rm A}$ was significantly lower than for the previous sample. A maximal temperature of around



167°C was reached. The scanning interval was set to $0-200\,\mathrm{amu}$ and the measurement time was set to $200 \, \frac{\text{ms}}{\text{amu}}$. The detected masses were $18 \, \text{amu}$, $2 \, \text{amu}$ and 44 amu. 18 amu most likely corresponds to H₂O, which probably originates from residual water on the target holder. The 2 amu detection could be consistent with the presence of D in the sample, either through implantation or binding. However, it is also possible that 2 amu corresponds to H_2 , which comes from contamination. Given that neither 1 amu (H) nor 4 amu (D₂) was present during the heatramp, no further conclusions can be drawn. The third detected mass, $44 \,\mathrm{amu}$, is CO_2 due to the presence of both carbon and oxygen in the sample. The elements are visible in the ion current over temperature visualization in Figure 24. The measured ion current corresponding to H₂O was an order of magnitude higher than for the other elements.

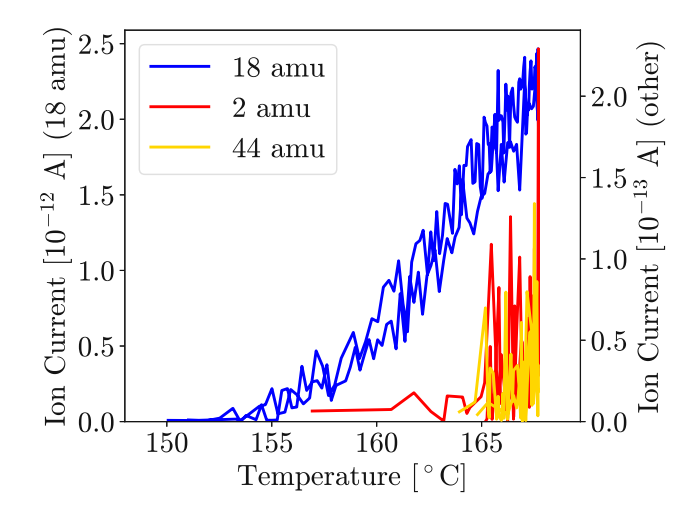


Figure 24: The ion current at specific masses plotted against the recorded temperature with the thermocouple. Three different masses with 18 amu, 2 amu and 44 amu occurred at temperature over 150°C during this heatramp.



$5.5 \text{ W:B} \approx 1:4$

5.5.1 Sputter yield

Given the elevated boron content of the sample, it was anticipated that a greater duration would be required to attain a steady state per angle step. This hypothesis was confirmed by the experimental data, which showed that a beamtime of 1800 s was required for the argon measurements and 10800s for the deuterium measurements. The applied heating current of $I_h = 1.82 \,\mathrm{A}$ lead to a recorded temperature of 110°C for the deuterium measurements.

The results for the sputter yield measurements are shown in Figure 25. The argon yield, displayed on the left-hand side of the figure, is higher than the simulation. This is an unusual occurrence, as in the past, simulations had a tendency to overestimate the yield. The measured yield for deuterium, displayed on the right of the figure, is again lower than predicted by the simulation. Both curves indicate an amorphous target structure. $\approx 1.7 \cdot 10^{21} \frac{Ar^+}{m^2}$ and $\approx 1.3 \cdot 10^{22} \frac{D_2^+}{m^2}$ have been applied to this sample. This is approximately the same fluence that was applied to the pure boron sample (section 5.2).

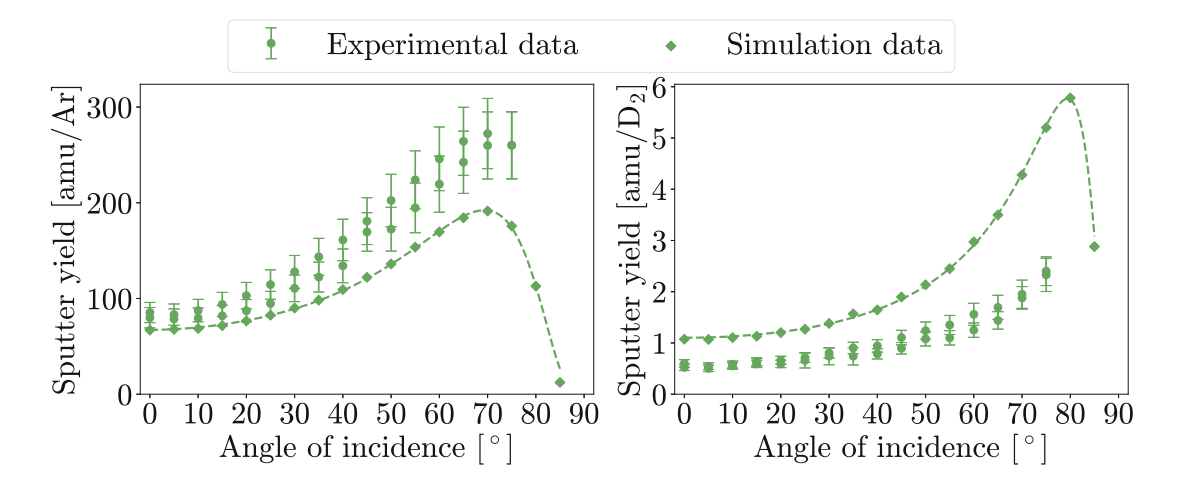


Figure 25: Experimental sputter yield of the W:B ≈ 1.4 sample irradiated with $2\,\mathrm{keV}\,\mathrm{Ar}^+$ ions at the left and $2\,\mathrm{keV}\,\mathrm{D}_2^+$ ions at the right compared with SDTrimSP simulations.

5.5.2 Surface changes

Table 5.9 and Table 5.10 show the surface recorded with the AFM and the respective values for the surface properties. The decreased values for $R_{\rm q}$ and $\delta_{\rm m}$ in the irradiated area indicate, that a smoothing of the surface seems to happen during irradiation. This behavior is similar to that observed for the pure boron sample described in section 5.2.

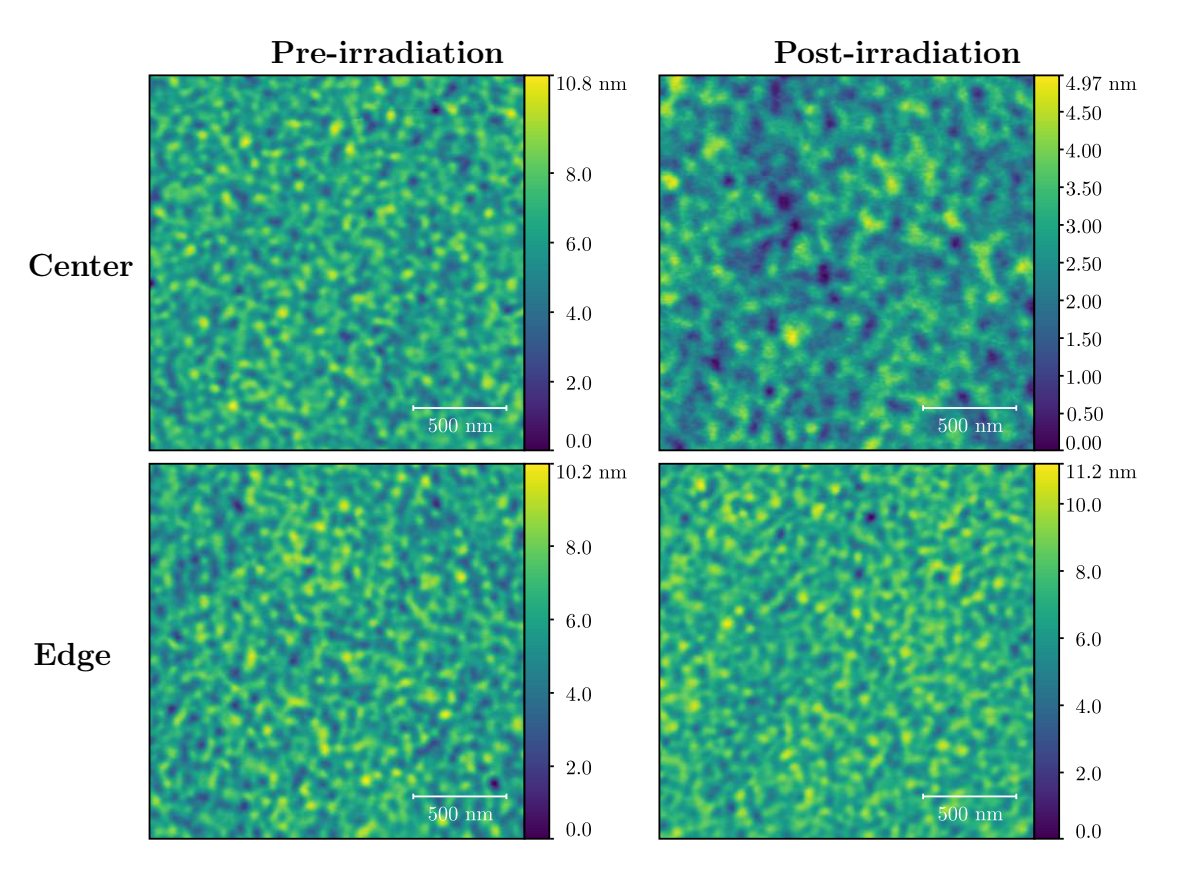


Table 5.9: AFM images for the W:B \approx 1:4 sample before and after irradiation for irradiated area (center) and non-irradiated area (edge).

	Pre-irradiation	Post-irradiation
$R_{\rm q}$ center [nm]	1.21	0.67 ± 0.02
$R_{\rm q}$ edge [nm]	1.26 ± 0.03	1.12 ± 0.05
$\delta_{\rm m}$ center [deg]	3.59	1.77 ± 0.23
$\delta_{\rm m}$ edge [deg]	3.83 ± 0.31	3.38 ± 0.24

Table 5.10: Values for the RMS roughness and mean inclination angle before and after irradiation for the W:B \approx 1:4 sample.

5.5.3 QMS measurements

A fluence of $2.3 \cdot 10^{21} \, \frac{D_2^+}{m^2}$ was applied to the sample. The irradiation happened at a recorded temperature of 36° because the filament of the QMS was already switched on. After sufficiently low pressure, a heatramp with $t_{\text{ramp}} = 3 \,\text{h}$, $I_{\text{max}} = 3.5 \,\text{A}$ and $t_{\text{hold}} = 1 \,\text{h}$ was started. A maximal temperature of around 209°C was recorded. For this heatramp a scanning interval of $0-200\,\mathrm{amu}$ and a measurement time of $200 \frac{\text{ms}}{\text{amu}}$ were chosen. The results are shown in a QMS ion current over temperature plot in Figure 26.

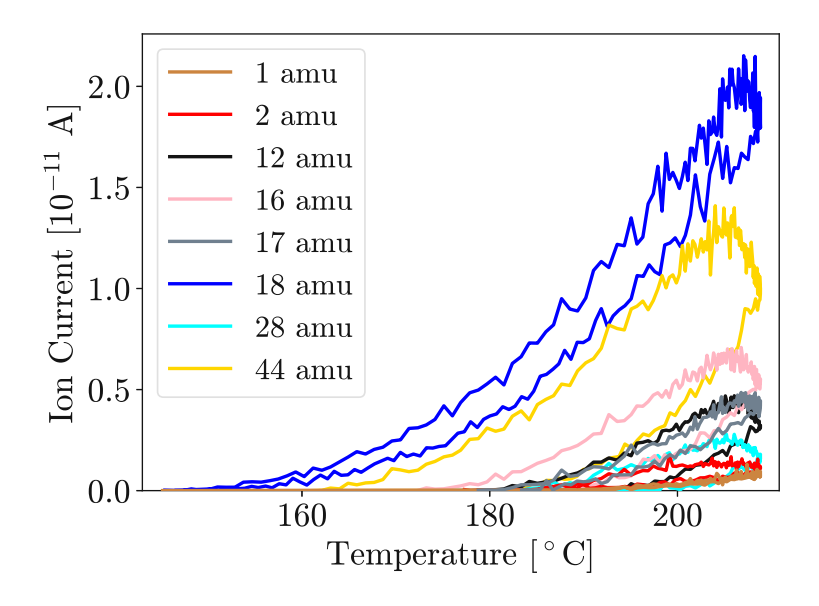


Figure 26: The ion current for specific masses plotted against the temperature recorded with the thermocouple for the W:B ≈ 1.4 sample.

In total 8 different mass numbers could be identified during the heatramp. Almost all mass numbers can be attributed to elements within the W:B \approx 1:4 sample. 1 amu could correspond to H, 2 amu to either D or H₂, 12 amu to C, 16 amu to O, 17 amu to OH, 18 amu to H₂O, 28 amu to N₂ and 44 amu to CO₂. In this heatramp, the presence of both 1 amu and 2 amu was detected simultaneously. This finding indicates that the recorded 2 amu element is more likely to correspond to H₂ than D.

5.6 Comparison and summary

This section compares and summarizes the results obtained for the sputter yield, surface changes and QMS measurements. In addition, the sputter yield plots are presented in different ways, e.g. yield versus boron concentration or in units of atoms/ion, to give more information about possible trends.

The conversion from amu/ion to atoms/ion is made under the assumption that a steady state sputter yield has been reached and the equation

$$\frac{Y_{\text{W,at}}}{Y_{\text{B,at}}} = \frac{q_{\text{W}}}{q_{\text{B}}} \tag{5.2}$$

applies [45]. $Y_{\text{W,at}}$ and $Y_{\text{B,at}}$ represent the steady state sputter yield of the respective elements in atoms/ion whereas q_{W} and q_{B} represent the elemental concentrations given in Table 4.1. With Equation 5.2 and the measured total yield $Y_{\text{tot,amu}} = Y_{\text{W,at}} \cdot m_{\text{W}} + Y_{\text{B,at}} \cdot m_{\text{B}}$ in amu/ion the partial sputter yields

$$Y_{\text{B,at}} = \frac{Y_{\text{tot,amu}}}{\frac{q_{\text{W}}}{q_{\text{B}}} \cdot m_{\text{W}} + m_{\text{B}}}, \qquad Y_{\text{W,at}} = \frac{Y_{\text{tot,amu}}}{\frac{q_{\text{B}}}{q_{\text{W}}} \cdot m_{\text{B}} + m_{\text{W}}}$$
(5.3)

can be calculated. $m_{\rm W}$ and $m_{\rm B}$ denote the atomic masses of tungsten and boron. To convert the yield for the compound samples the concentration values from Table 4.1 were taken. To calculate the yield in atoms per ion for the pure samples, compositions of 100% tungsten and 100% boron were assumed, respectively.

5.6.1 Sputter yield

Argon measurements

Figure 27 displays the inverse-variance weighted mean values of the measurement points for the argon measurements that were introduced in the previous sections. Eckstein fits have been utilized to guide the eye. The fits work very well for all targets that give an amorphous structure. However, the Eckstein fit does not describe the crystal nature of pure tungsten very well and therefore a spline is

used to describe the curve of the pure tungsten sample. For all samples except the pure tungsten sample, a clear trend towards a lower sputter yield can be identified for higher boron concentrations.

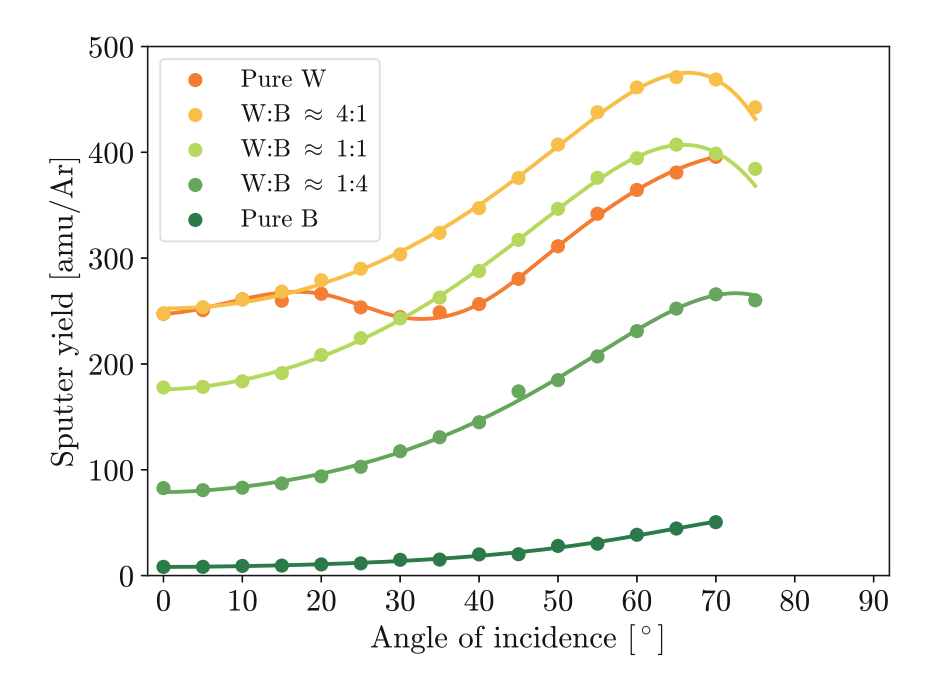


Figure 27: Sputter yield of 2 keV Ar⁺ irradiation as a function of the angle of incidence. Eckstein fits were applied to the measured data points with the exception of pure W, where a spline is used.

Figure 28 provides a comparison of the simulated sputter yield. A trend towards lower sputter yield can be observed for higher boron concentrations. In this visualization, only the amorphous tungsten simulation is shown to enhance comparability to the simulations for the other samples. Again, Eckstein fits are applied to enhance the visibility of the curve. The experimentally measured yield for the pure tungsten sample is lower than the yield for the W:B $\approx 4:1$ sample, even though the simulation would suggest a higher yield. For some points, one potential explanation for this phenomenon could be attributed to the crystalline structure of the target, which could lower the measured yield in comparison to an amorphous target. Nonetheless, this is not applicable to every data point and the matter is therefore still under investigation.



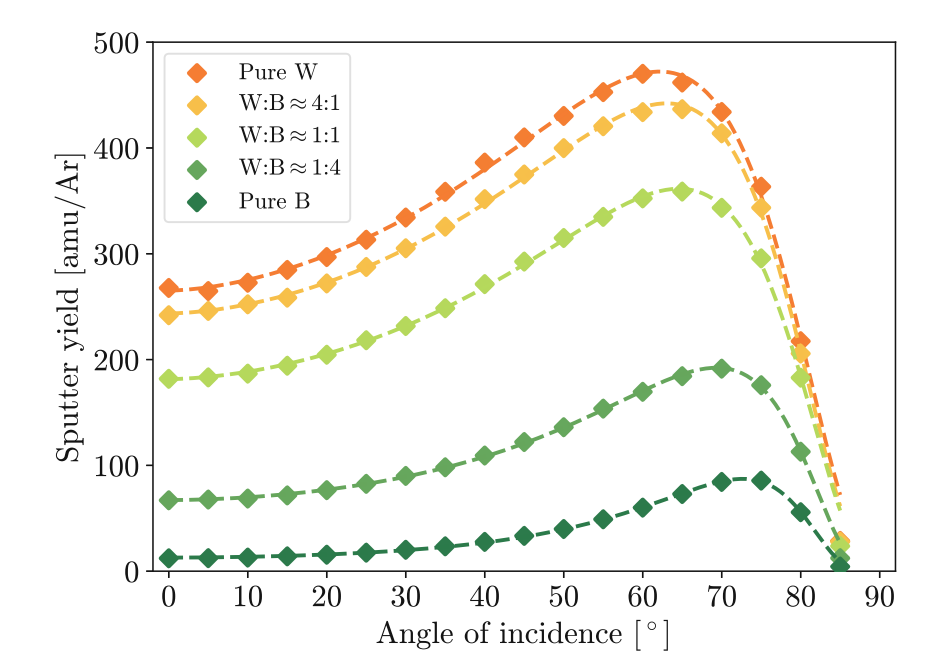


Figure 28: Simulated sputter yield of 2 keV Ar⁺ irradiation as a function of the angle of incidence. Eckstein fits have been applied to give a better visualization of the trend.

To visualize the dependence of the yield over the boron concentration for a few selected angles, additional plots have been made (see Figure 29). One can see different trends when looking at the two figures. In the left figure, when considering the yield in amu/Ar, a tendency towards a lower amount of mass removed can be seen for higher boron concentrations. In the right figure, the sputter yield in B/Ar is provided by the solid lines (right vertical axis) and the sputter yield in W/Ar is provided by the dashed lines (left vertical axis). With increasing boron concentration, the amount of sputtered tungsten particles decreases and the amount of sputtered boron particles increases. One exception is the pure boron sample, where the amount of boron particles decreases again in comparison to the W:B ≈ 1.4 sample. This might come from the fact that pure boron acts as a much better oxygen getter than samples with lower boron concentration. Therefore, it is possible that this improved gettering reduces the yield of the pure sample compared to compound samples. The measurement could be repeated at an elevated temperature to potentially suppress the gettering effect.



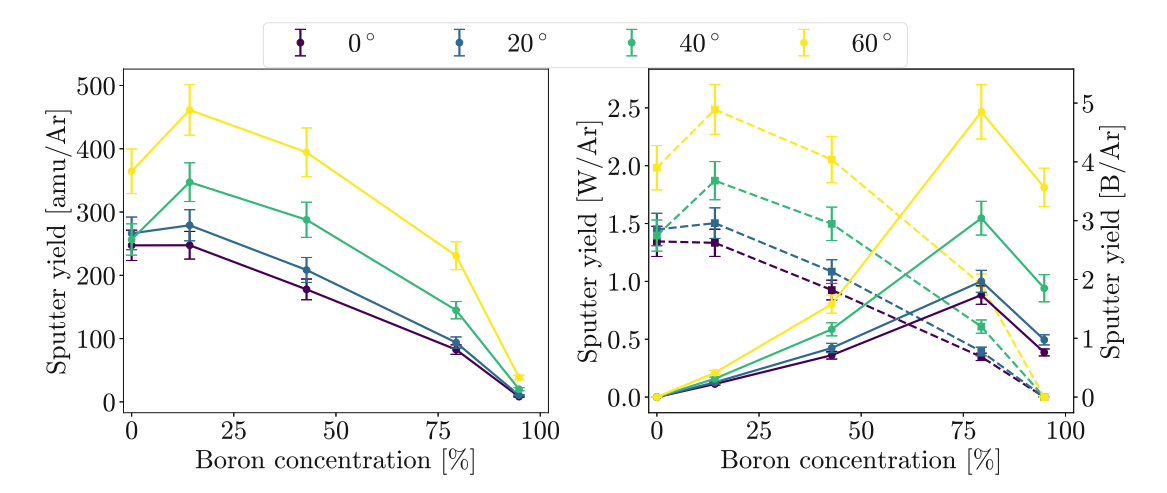


Figure 29: The sputter yield as a function of the boron concentration for different angles of incidence. The left side shows the yield in terms of amu/Ar, whereas the right side displays it in B/Ar for the solid lines and in W/Ar for the dashed lines.

For a nuclear fusion reactor one important quantity is the amount of high-Z particles that are sputtered from the wall. The data indicates that with increasing boron concentration, the total amount of particles sputtered by the impact of argon increases. Simultaneously however, increasing boron concentration reduces the amount of high-Z particles. Consequently, it can be deduced that a boron layer functions as a protective coating for the tungsten wall, reducing the number of high-Z atoms ejected into the plasma under 2 keV Ar⁺ irradiation. It should be stressed however, that this conclusion is only valid for argon energies of 2 keV. In a fusion reactor, particles are not monoenergetic.

Deuterium measurements

For the deuterium measurements, a figure displaying the inverse variance-weighted mean values of the yield for all samples is visible in Figure 30. Figure 31 shows the comparison of the associated simulated yield. Again, Eckstein fits have been applied to the data points with the exception of pure W, where a spline is used.

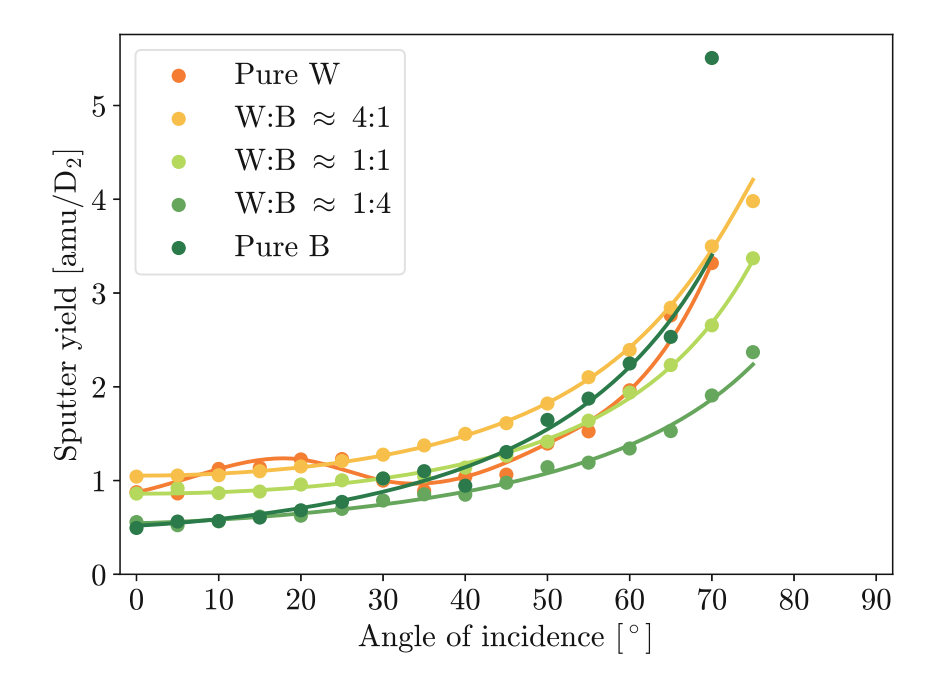


Figure 30: Sputter yield of $2 \,\mathrm{keV}\,\mathrm{D_2}^+$ irradiation for different samples with respect to the angle of incidence. Eckstein fits were applied to the measured data points with the exception of pure W, where a spline is used.

It is visible that the differences in sputter yield are not very large. However, the trend for the experiment and the simulation agrees for most parts. The compound samples show a decrease in sputtered mass with increasing boron concentration both in the simulation and in the experiment. The measured yield in amu/ D_2 for the pure boron sample starts in the range of the W:B ≈ 1.4 sample, but rises rapidly to exceed the measured yield of the W:B $\approx 1:1$ sample after 55°. This is almost consistent with the prediction of the simulation, where the pure boron yield overtakes the W:B ≈ 1.1 yield at 60°. However, according to the simulation, the yield of pure boron sample should only be higher than the yield of the W:B ≈ 1.4 sample at around 50° and not directly in the beginning. In the simulation, the yield for pure tungsten and W:B ≈ 4.1 is almost identical. This is true experimentally for the data between 10° and 25°. For the rest of the pure tungsten data, the yield is significantly lower than predicted, similar to the argon case. Again,

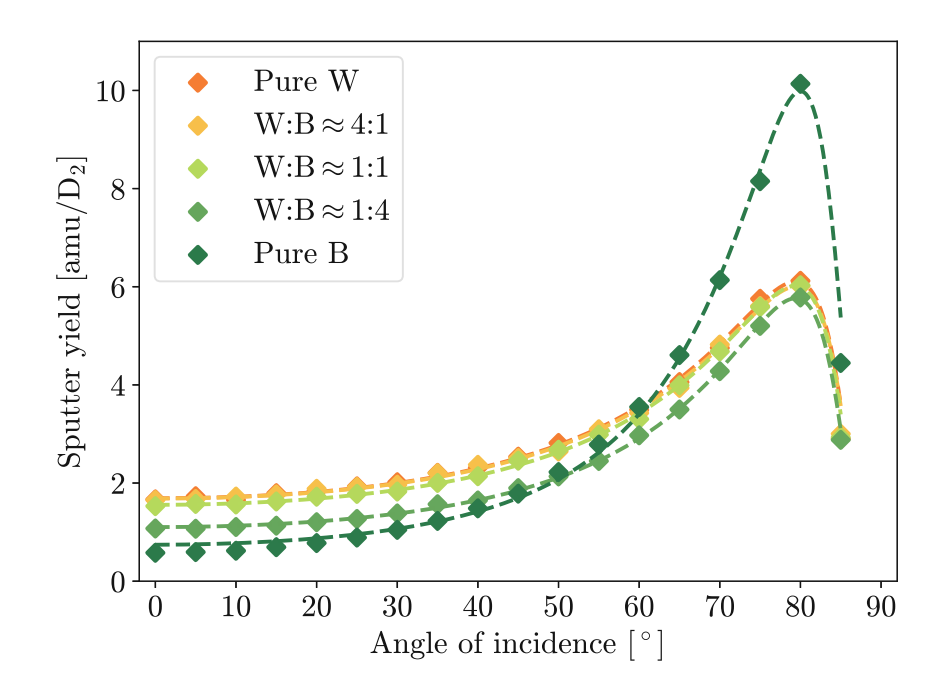


Figure 31: Simulated sputter yield of 2 keV D₂⁺ irradiation for different samples with respect to the angle of incidence. Eckstein fits have been applied to give a better visualization of the trend.

the crystal structure might cause lower yield for single data points. However, this is still under investigation and does not provide a satisfactory explanation for the rest of the data points.

Once more, the sputter yield data for deuterium bombardment is also shown as a function of the boron concentration (see Figure 32). In terms of amu/ D_2 a small trend towards lower sputtered mass can be seen for increasing boron concentration with the exception of almost pure boron. In this case, the yield seems to increase, with the increase being dependent on the angle. The yield exhibits an increase with increasing angle, with higher angles resulting in a more pronounced increase. Compared to the argon measurements however, the amount of removed mass did not vary as much with increasing boron concentration. Converting the yield into W/D_2 and B/D_2 , different trends can be observed. visible in Figure 32. The dashed line represents the sputter yield in W/D_2 and the solid line in B/D_2 . Almost identical to the argon case, a decreasing amount of tungsten particles and an increasing amount of boron particles is sputtered with increasing boron concentration. A very steep increase in B/D_2 is recorded transitioning from W:B \approx 1:4 to a pure boron sample.

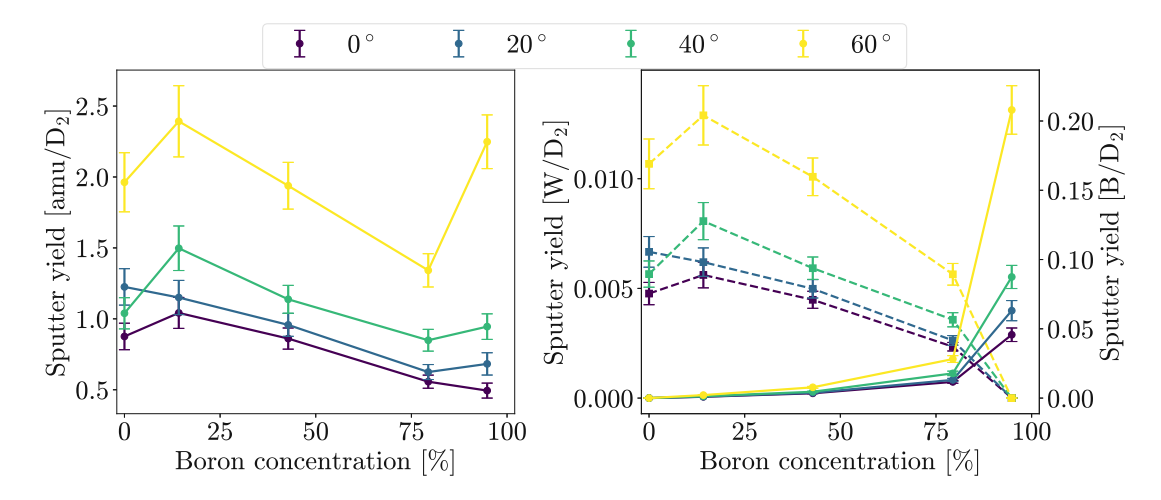


Figure 32: The sputter yield as a function of the boron concentration for different angles of incidence. The left side shows the yield in terms of amu/ D_2 , whereas the right side displays it in B/D₂ for the solid lines and in W/D_2 for the dashed lines.

In a fusion reactor, an increase in boron concentration on the wall would result in the emission of an order of magnitude more particles into the plasma, as can be deduced from the right of Figure 32. However, the eroded particles would correspond to boron, a low-Z material. Consequently, the eroded particles would not pose the same level of threat to the plasma as high-Z materials, such as tungsten.

5.6.2 Surface changes

Before summarizing the surface changes, it has to be mentioned that the following interpretations rely on very little statistics. 1-3 spots for each irradiated and nonirradiated area were made per sample. These spots were chosen randomly over the desired area and function as a reference for the entire area. However, strictly speaking, the changes in surface properties are only valid for the inspected spots. To quantify the changes that occur or do not occur in surface properties, one must first consider the applied ion fluences, which are summarized in Table 5.11. Additionally, the changes of the surface is indicated in the last column.

Die app	The ap
3ibliothek	Your knowledge hub
2	N E N

	Ar^+ fluence $\left[10^{20} \frac{ions}{m^2}\right]$	D_2^+ fluence $\left[10^{21} \frac{\rm ions}{\rm m^2}\right]$	Surface changes
Pure W	1.3	6	None
W:B $\approx 4:1$	9.6	5.1	Roughening
W:B $\approx 1:1$	6	6.2	None
W:B $\approx 1:4$	17	13	Smoothing
Pure B	27	12	Smoothing

Table 5.11: Total ion fluences applied to the different samples and observed changes of the surface.

Despite the fact that the fluence of the D_2^+ ions is one order of magnitude higher than that of the Ar^+ ions, changes in surface properties are most likely attributable to the bombardment with argon. This is attributable to the fact that the sputter yield induced by argon ions in terms of atoms/ion is more than one order of magnitude higher than for deuterium.

It was not possible to observe surface changes for the pure W and W:B≈ 1:1 samples (section 5.1 and section 5.3). In contrast, surface changes were observed for all other samples. The irradiated surface roughened in case of the W:B \approx 4:1 sample (section 5.4), but smoothened for the W:B $\approx 1:4$ and pure B sample (section 5.5 and section 5.2). It is possible that the surface changes are a function of the applied fluence. This conclusion would be in agreement with the experimental findings, because in both cases with the lowest applied fluence, no detectable surface changes occurred. It appears that an initial roughening of the surfaces is followed by a subsequent smoothing of the surfaces at higher fluence levels. However, it is important to consider the possibility that the varying boron concentrations of the samples could also contribute to this effect. When considering compound samples, preferential sputtering can occur. This phenomenon occurs when one species of atoms within a compound material is more prone to sputtering compared to other species. If preferential sputtering occurred for these samples and how its occurrence is related to the surface properties is still under investigation.

5.6.3 QMS measurements

A summary of the measurements with the quadrupole mass spectrometer can be seen in Table 5.12. It shows the mass number and the most probable elements occurring in the heatramps for each sample.

S	
P	
7	q
t	e h
.0	edg
	NO.
끋	돧
M	ζ
\supset	Z H

Mass [amu]	1	2	12	16	17	18	28	44
Element	Н	${ m H_2/D}$	\mathbf{C}	Ο	ОН	H_2O	N_2	CO_2
$W:B \approx 4:1$		√				√		\checkmark
$W:B \approx 1:1$						\checkmark		
$W:B \approx 1:4$	√	\checkmark						

Table 5.12: Summary of the QMS measurements and occurring masses for the different samples.

Every mass that was detected with the QMS can either be found within the initial sample composition visible in Table 4.1, was potentially implanted (deuterium) or originates from contamination (water). Given that the 2 amu signal only appeared simultaneously with the 1 amu signal, it is more likely that the 2 amu corresponds to H_2 , originating from contamination.

The reason why only water was visible in the heatramp for the W:B \approx 1:1 sample is not entirely clear. One explanation might be that this was the second heatramp that was applied to this sample without additional irradiation in between the heatramps. If the 2 amu element indeed corresponded to D, all implanted or bonded deuterium could have already outgassed from the sample before conducting this heatramp. This, however, does not provide a satisfactory explanation for the absence of elements identified within the first heatramp for this sample. One potential explanation for this could be that the fluence applied to this sample was the lowest in comparison to the other heatramps or the amount of outgassing elements were below the detection limit of the QMS.

Conclusion and outlook

A comprehensive understanding of the influence of boron on the erosion properties of the first wall is crucial for the successful operation of nuclear fusion devices. The deposition of boron on a full tungsten wall is a consequence of the boronization process, which is utilized in fusion reactors to reduce impurities in the plasma. This study demonstrated that the amount of boron deposited on the wall has a direct effect on its erosion properties.

Within the scope of this thesis a quartz crystal microbalance setup was utilized to successfully determine angle resolved sputter yields with $2\,\mathrm{keV}\,\mathrm{Ar}^+$ and subsequent $2 \,\mathrm{keV} \,\mathrm{D}_2^+$ ions for a total of five samples with different tungsten-boron mixing ratios. For the first time, a comparison of the experimental yield was conducted with SDTrimSP simulations that allow crystal structures as an input. In order to gain insight into potential surface changes that occurred during irradiation, atomic force microscope images were taken before and after bombardment. The root-mean-square roughness $R_{\rm q}$ and the mean of the surface inclination angle distribution $\delta_{\rm m}$ were selected as indicators for potential alterations. Observations indicate that surface alterations occur during irradiation as a function of the applied ion fluence and the boron concentration in the sample. It has been found that at higher fluences and boron concentrations, the surface undergoes a smoothing process. Furthermore, a quadrupole mass spectrometer was added to the experimental setup after measurements with the pure boron sample were conducted. It was used to determine outgassing elements from the compound samples.

During the measurement of the pure boron sample, it was found that deuterium measurements could not be conducted at room temperature. It is hypothesized that a binding of deuterium to boron may occur during the process of irradiation. To circumvent this potential interaction, D₂ measurements were conducted on samples containing boron at elevated temperatures, with a minimum of 104°C being maintained. QMS measurements showed that two out of the three compound samples release an element with 2 amu during heating, indicating the presence of either D or H₂. As 4 amu was not present in the heatramps, but 1 amu was in one heatramp, the presence of H₂ seems more likely. However, this still requires further investigation.

A comparison of experimental sputter yield, obtained in both argon and deuterium measurements, with crystalline SDTrimSP simulations strengthened the suspicion of a texture effect occurring in the pure tungsten sample, which was observed experimentally in the past [18]. In all other samples, amorphous structures were observed experimentally, obtainable from the slope of the yield over angle curve.

In general, the experiments with argon showed that less mass is sputtered with increasing boron concentration. Simultaneously, the amount of boron particles increased and the amount of tungsten particles decreased with increasing boron concentration. A comparison with simulations regarding the argon measurement reveals excellent agreement to experiments for samples with lower boron content, with the exception of the pure tungsten sample most likely due to its crystalline nature. A slight offset between simulation and experiment for the two samples with the highest boron content were observed.

The tendency towards lower mass removed per impinging ion with higher boron concentration was not as pronounced in the deuterium measurements. Nevertheless, a weak trend was still detectable. Converting the yield into W/D₂ and B/D₂ a comparable trend to the argon measurement was visible. This leads to the conclusion that the atoms eroded by deuterium from a fully boron coated wall would be lighter, but greater in number compared to a tungsten wall. With the exception of pure boron, all comparisons of experimental data and simulated data for deuterium showed an offset, with the experimental data being lower than predicted by the simulation. One potential explanation for this discrepancy could be attributed to the diffusion parameters employed in the simulation, which are not based on experimental observations but on an initial guess.

In summary, it can be said that a boron coated tungsten wall would, besides of being an excellent oxygen getter, have an additional advantage over a pure tungsten wall under 2 keV Ar^+ and 2 keV D_2^+ irradiation in a nuclear fusion device. This is evidenced by the reduction in the emission of high-Z materials into the plasma due to the decreasing amount of sputtered tungsten with increasing boron concentration.

58

Bibliography

- Mikhaylov, A., Moiseev, N., Aleshin, K. & Burkhardt, T. Global climate change and greenhouse effect. Entrepreneurship and Sustainability Issues 7, 2897 (2020).
- Anderson, T. R., Hawkins, E. & Jones, P. D. CO2, the greenhouse effect and global warming: from the pioneering work of Arrhenius and Callendar to today's Earth System Models. Endeavour 40, 178–187 (2016).
- Ritchie, H. & Roser, M. CO emissions. Our World in Data. https://ourwo rldindata.org/co2-emissions (2020).
- Ritchie, H. & Rosado, P. Electricity Mix. Our World in Data. https://our worldindata.org/electricity-mix (2020).
- Demtröder, W. Experimentalphysik 4: Kern-, Teilchen-und Astrophysik (Springer-Verlag, 2017).
- 6. Chen, F. F. et al. Introduction to plasma physics and controlled fusion (Springer, 1984).
- Wesson, J. & Campbell, D. J. Tokamaks (Oxford university press, 2011).
- IPP Magnetic confinement https://www.ipp.mpg.de/15072/mageinschl uss. Accessed: 2024-05-10.
- ITER cross section https://www.iter.org/mach/Tokamak. Accessed: 2024-05-27.
- Neu, R. et al. Plasma wall interaction and its implication in an all tungsten 10. divertor tokamak. Plasma Physics and Controlled Fusion 49, B59 (2007).
- Dibon, M. et al. New boronization system at ASDEX Upgrade. Fusion Engineering and Design 165, 112233 (2021).
- Oxygen gettering properties of boron film produced by diborane dc glow discharge. Journal of Nuclear Materials 248, 38-41. ISSN: 0022-3115. https ://www.sciencedirect.com/science/article/pii/S0022311597001141 (1997).
- Winter, J. et al. Boronization in TEXTOR. Journal of Nuclear Materials **162**, 713–723 (1989).

- Boronization in DIII-D. Journal of Nuclear Materials 196-198. Plasma-Surface Interactions in Controlled Fusion Devices, 236–240. ISSN: 0022-3115. https://www.sciencedirect.com/science/article/pii/S002231150680 0383 (1992).
- 15. Skinner, C. et al. Effect of boronization on ohmic plasmas in NSTX. Nuclear fusion 42, 329 (2002).
- Kallenbach, A. et al. Non-boronized compared with boronized operation of ASDEX Upgrade with full-tungsten plasma facing components. Nuclear Fusion 49, 045007 (2009).
- Cupak, C. Influence of roughness on sputter yields of tungsten-dcoatings rel-17. evant for nuclear fusion devices Diploma Thesis, TU Wien. (2019).
- 18. Fellinger, M. Investigation of sputtering properties of tungsten model systems relevant for nuclear fusion devices Diploma Thesis, TU Wien. (2022).
- 19. Cupak, C. et al. Sputter yields of rough surfaces: Importance of the mean surface inclination angle from nano-to microscopic rough regimes. Applied Surface Science **570**, 151204 (2021).
- 20. Stadlmayr, R. et al. A high temperature dual-mode quartz crystal microbalance technique for erosion and thermal desorption spectroscopy measurements. Review of Scientific Instruments 91, 125104. ISSN: 0034-6748 (Dec. 2020).
- 21. Sauerbrey, G. Verwendung von Schwingquarzen zur Wägung dünner Schichten und zur Mikrowägung. Zeitschrift für Physik 155, 206–222 (1959).
- 22. Hayderer, G., Schmid, M., Varga, P., Winter, H. & Aumayr, F. A highly sensitive quartz-crystal microbalance for sputtering investigations in slow ionsurface collisions. Review of Scientific Instruments 70, 3696–3700 (1999).
- Stevens, D. & Tiersten, H. An analysis of doubly rotated quartz resonators 23. utilizing essentially thickness modes with transverse variation. The Journal of the Acoustical Society of America 79, 1811–1826 (1986).
- Szabo, P. S. Experimental and simulated sputtering of Gold, Iron and Wollastonite with a Catcher-QCM setup PhD thesis (Technische Universität Wien, 2017).
- Mutzke, A. et al. SDTrimSP Version 7.02 (2024). 25.
- Eckstein, W. Computer simulation of ion-solid interactions (Springer Science & Business Media, 2013).
- Urano, H. et al. Roles of argon seeding in energy confinement and pedestal structure in JT-60U. *Nuclear Fusion* **55**, 033010 (2015).

- 28. Schmid, Μ. Möglichkeiten und Grenzen der Schwingquarz-Schichtdickenmessung. Doctoral Dissertation, TU Wien (1989).
- Redl, A. Creation of a Python-based control software for QCM measurements and implementation of a real-time GUI for data acquisition. Project Thesis, TU Wien (2022).
- 30. Virtanen, P. et al. SciPy 1.0: Fundamental Algorithms for Scientific Computing in Python. *Nature Methods* **17**, 261–272 (2020).
- Wolfgang, P. & Helmut, S. Apparatus for separating charged particles of different specific charges. US Patent 2,939,952 (June 1960).
- 32. Binnig, G., Quate, C. F. & Gerber, C. Atomic force microscope. *Physical* Review Letters **56**, 930 (1986).
- Garcia, R. & Perez, R. Dynamic atomic force microscopy methods. Surface 33. Science Reports 47, 197–301 (2002).
- Seo, Y. & Jhe, W. Atomic force microscopy and spectroscopy. Reports on 34.Progress in Physics **71**, 016101 (2007).
- Szabo, G. L. Electronic excitation and momentum transfer driven surface modifications by ion impacts PhD thesis (Technische Universität Wien, 2023).
- Lundin, D., Minea, T. & Gudmundsson, J. T. High power impulse magnetron 36. sputtering: fundamentals, technologies, challenges and applications (2019).
- Ström, P., Petersson, P., Rubel, M. & Possnert, G. A combined segmented anode gas ionization chamber and time-of-flight detector for heavy ion elastic recoil detection analysis. Review of Scientific Instruments 87, 103303. ISSN: 0034-6748 (Oct. 2016).
- Pitthan, E., Moro, M., Corrêa, S. & Primetzhofer, D. Assessing boron quantification and depth profiling of different boride materials using ion beams. Surface and Coatings Technology 417, 127188. ISSN: 0257-8972 (2021).
- Bakhit, B. et al. Systematic compositional analysis of sputter-deposited boron-containing thin films. Journal of Vacuum Science Technology A 39, 063408. ISSN: 0734-2101 (Sept. 2021).
- Eckstein, W. & Preuss, R. New fit formulae for the sputtering yield. Journal 40. of Nuclear Materials **320**, 209–213 (2003).
- Herzberg, G. & Monfils, A. The dissociation energies of the H2, HD, and D2 molecules. Journal of Molecular Spectroscopy 5, 482–498 (1961).
- 42. Brötzner, J. et al. Sputtering yield reduction for nano-columnar W surfaces under D ion irradiation. Nuclear Materials and Energy 37, 101507 (2023).

- Eckstein, W., Garcia-Rosales, C., Roth, J. & Ottenberger, W. Sputtering 43. data (1993).
- Fellinger, M. To be published (2025). 44.
- Wilhelm, R. A. Ion-Solid Interaction Lecture notes, TU Wien. 2022. 45.

TU **Bibliothek**, Die approbierte gedruckte Originalversion dieser Diplomarbeit ist an der TU Wien Bibliothek verfügbar wien vour knowledge hub. The approved original version of this thesis is available in print at TU Wien Bibliothek.

List of Figures

1	fuels and industry. Taken and adapted from [3]	1
2	An overview of the global energy production by individual sources. Taken and adapted from [4]	2
3	Average binding energy per nucleon as a function of nucleon number. Taken and adapted from [5]	ć
4	Visual representation of the deuterium-tritium fusion	4
5	Principle of magnetic confinement in a tokamak. Taken and adapted from [8]	Ę
6	Cross-sectional view of ITER with the divertor and the first wall highlighted. Taken and adapted from [9]	6
7	Illustration of the QCM setup	Ć
8	Sensitivity of a quartz used in this thesis as a function of distance from the center. Data taken from [24]	10
9	Schematic of the QSPARX experimental setup. Taken and adapted from [18]	14
10 11	Visualization of the QCM control loop	15 16
12	Exemplary case of a measured sputter yield as a function of the applied ion fluence with an exponential fit applied.	19
13	Visualization of the AFM measurement principle	21
14	A visualization of the interaction potential between neutral atoms including associated AFM operation modes. The different regions	96
	are approximated from [35]	22
15	Concentration over depth values for the five investigated samples. The depth ranges taken for the calculation of the mean concentration values are marked in gray	25
	ordin various are marked in gray	ے و

16	Experimental sputter yield of the pure tungsten sample irradiated with 2 keV Ar^+ ions at the left and 2 keV D_2^+ ions at the right compared with data from [18] [19] [43]	30
17	Experimental sputter yield of the pure tungsten sample irradiated with 2keV Ar^+ ions at the left and 2keV D_2^+ ions at the right compared with simulations from SDTrimSP. Additionally to a dynamic amorphous target simulation, static crystalline structures with indicated crystal orientation are shown in the plots	30
18	Part of the $2\mathrm{keV}\mathrm{Ar}^+$ frequency curve during the measurement. Δf denotes the difference between the eigenfrequency f_0 at the measurement start and the frequency at a given time during the measurement.	33
19	Experimental sputter yield of the pure boron sample irradiated with $2 \mathrm{keV} \mathrm{Ar}^+$ ions at the left and $2 \mathrm{keV} \mathrm{D}_2^+$ ions at the right compared with simulations from SDTrimSP	34
20	Part of the $2 \text{ keV } D_2^+$ frequency curve during the measurement. Δf denotes the difference between the eigenfrequency f_0 at the start of the measurement and the present frequency at a given time	35
21	Experimental sputter yield of the W:B \approx 1:1 sample irradiated with 2keV Ar^+ ions at the left and 2keV D_2^+ ions at the right compared with SDTrimSP simulations	38
22	The QMS ion current plotted over the temperature during the heatramp. The only detectable element had mass number 18, most likely corresponding to H_2O	41
23	Experimental sputter yield of the W:B \approx 4:1 sample irradiated with 2keV Ar^+ ions at the left and 2keV D_2^+ ions at the right compared with SDTrimSP simulations	42
24	The ion current at specific masses plotted against the recorded temperature with the thermocouple. Three different masses with 18 amu, 2 amu and 44 amu occurred at temperature over 150°C dur-	
25	ing this heatramp	4445
26	The ion current for specific masses plotted against the temperature recorded with the thermocouple for the W:B \approx 1:4 sample	47
27	Sputter yield of 2 keV Ar ⁺ irradiation as a function of the angle of incidence. Eckstein fits were applied to the measured data points with the exception of pure W, where a spline is used	49

Die appro The appro	
Sibliothek , Your knowledge hub	

28	Simulated sputter yield of 2 keV Ar ⁺ irradiation as a function of the	
	angle of incidence. Eckstein fits have been applied to give a better	
	visualization of the trend	50
29	The sputter yield as a function of the boron concentration for dif-	
	ferent angles of incidence. The left side shows the yield in terms	
	of amu/Ar, whereas the right side displays it in B/Ar for the solid	
	lines and in W/Ar for the dashed lines	51
30	Sputter yield of 2 keV D_2^+ irradiation for different samples with	
	respect to the angle of incidence. Eckstein fits were applied to the	
	measured data points with the exception of pure W, where a spline	
	is used	52
31	Simulated sputter yield of 2 keV D_2^+ irradiation for different sam-	
	ples with respect to the angle of incidence. Eckstein fits have been	
	applied to give a better visualization of the trend	53
32	The sputter yield as a function of the boron concentration for dif-	
	ferent angles of incidence. The left side shows the yield in terms	
	of amu/ D_2 , whereas the right side displays it in B/D_2 for the solid	
	lines and in W/D_2 for the dashed lines	54

List of Tables

4.1	Average sample compositions calculated from ToF-ERDA spectra in percent	24
4.2	Surface properties before irradiation	26
5.1	AFM images for the pure tungsten sample before and after irradiation for irradiated area (center) and non-irradiated area (edge)	32
5.2	Values for the RMS roughness and mean inclination angle before and after irradiation for the pure tungsten sample	32
5.3	AFM images for the pure boron sample before and after irradiation	
5.4	for irradiated area (center) and non-irradiated area (edge) Values for the RMS roughness and mean inclination angle before	37
- -	and after irradiation for the pure boron sample	37
5.5	AFM images for the W:B \approx 1:1 sample before and after irradiation for irradiated area (center) and non-irradiated area (edge)	39
5.6	Values for the RMS roughness and mean inclination angle before and after irradiation for the W:B $\approx 1:1$ sample	40
5.7	AFM images for the W:B \approx 4:1 sample before and after irradiation	
5.8	for irradiated area (center) and non-irradiated area (edge) Values for the RMS roughness and mean inclination angle before	43
	and after irradiation for the W:B \approx 4:1 sample	43
5.9	AFM images for the W:B \approx 1:4 sample before and after irradiation for irradiated area (center) and non-irradiated area (edge)	46
5.10	Values for the RMS roughness and mean inclination angle before	477
5.11	and after irradiation for the W:B \approx 1:4 sample Total ion fluences applied to the different samples and observed	47
T 10	changes of the surface	55
5.12	Summary of the QMS measurements and occurring masses for the different samples	56



Danksagung

Nach Abschluss meiner Matura im Sommer 2018 und vor Start meines Grundwehrdienstes im Jänner 2019 war ich auf der Suche nach einer Praktikumsstelle im Dafür habe ich unter anderem auch eine Bewerbung an die Bereich Physik. TU geschickt. Eines Tages habe ich dann einen Anruf von einem gewissen Herr Professor Friedrich Aumayr bekommen, der mich auf einen Besuch in die Arbeitsgruppe für Atom- und Plasmaphysik der TU eingeladen hat. Dort wurde ich freundlich (und mit Keksen) empfangen und nach einer Führung im Labor war mir sofort klar, dass ich dort mein Praktikum verbringen möchte. darauffolgenden Monate machten mir die Entscheidung, ob ich Physik an der TU studieren und den Kontakt zur Arbeitsgruppe aufrechterhalten wollte, leicht.

Diese Entscheidung habe ich bis heute nicht bereut und das habe ich größtenteils dir zu verdanken, lieber Fritz. Vielen Dank, dass du mich in diese Arbeitsgruppe aufgenommen und in das wissenschaftliche Arbeiten eingeführt hast. Dank dir konnte ich im Verlauf meines Praktikums, während meiner Bachelorarbeit und nun auch im Rahmen meiner Diplomarbeit wertvolle Erfahrungen sammeln sowie viele neue Kolleginnen und Kollegen kennenlernen und schätzen lernen. Hervorzuheben sind hierbei Anna, Janine, Gabriel, Herbert, Georg, Richard und Maria. Ihr hattet und habt zum Teil immer noch ein offenes Ohr für meine Fragen und Anliegen. Ein besonders großer Dank gebührt natürlich dir, liebe Martina. Du standest mir während meiner Diplomarbeit immer mit Rat und Tat zur Seite, nicht selten auch an eigentlich arbeitsfreien Tagen.

Während meines Studiums durfte ich viele neue Freundinnen und Freunde kennenlernen. Ich möchte mich besonders bei Michael, Florian und Paul be-Zu gut kann ich mich an die vielen gemeinsamen Lernsessions vor Prüfungen und das stundenlange Rechnen unserer Übungen erinnern. Ohne euch wäre das Studium nur halb so lustig gewesen.

Zuletzt möchte ich mich bei meiner Familie, insbesondern bei meinen Eltern, Romana und Günter, meinen Schwestern Franziska und Florentina und bei meinen Großeltern Christine, Gottfried und Hermine, bedanken. Danke, dass ihr es mir ermöglicht habt, meinen Interessen nachzugehen. Ich bin sehr froh, dass ihr hinter mir steht und mich weiterhin unterstützt.

